Non-canonical Telomerase Reverse Transcriptase Controls Osteogenic Differentiation of Aortic Valve Cells Through STAT5

Rolando A. Cuevas[1], Luis Hortells[1,2], Claire C. Chu[1], Ryan Wong[1], Alex Crane[1], Camille Boufford[1], Cailyn Regan[1], William J. Moorhead III[1], Michael J. Bashline[1], Aneesha Parwal[1], Angelina M. Parise[1], Aditi Gurkar[3], Dennis Bruemmer[4], John Sembrat[5], Ibrahim Sultan[6], Thomas G. Gleason[7], Marie Billaud[8], and Cynthia St. Hilaire[1,9*]

[1] Division of Cardiology, Department of Medicine, Pittsburgh Heart, Lung, Blood and Vascular Medicine Institute, University of Pittsburgh, Pittsburgh, Pennsylvania, USA.

[2] current address - Institute for Experimental Cardiovascular Medicine, University Heart Centre Freiburg–Bad Krozingen, Medical Center and Faculty of Medicine, University of Freiburg, Freiburg, Germany.

[3] Aging Institute, Division of Geriatrics, Department of Medicine, University of Pittsburgh, Pittsburgh, Pennsylvania, USA.

[4] Department of Cardiovascular Medicine, Cleveland Clinic, Cleveland, OH, USA.

[5] Division of Pulmonary, Allergy, and Critical Care Medicine, University of Pittsburgh School of Medicine, Pittsburgh, PA, USA.

[6] Division of Cardiac Surgery, Department of Cardiothoracic Surgery, Heart and Vascular Institute, University of Pittsburgh Medical Center, Pittsburgh, Pennsylvania, USA.

[7] Division of Cardiac Surgery, Univ. of Maryland School of Medicine, Baltimore, MD, USA.

[8] Department of Surgery, Division of Cardiac Surgery, Brigham and Women's Hospital & Harvard Medical School, Boston, Maryland, USA.

[9] Department of Bioengineering, University of Pittsburgh, Pittsburgh, Pennsylvania, USA.

Running Title: TERT/STAT5 is required for cardiovascular calcification

*Corresponding Author Contact Info:
Cynthia St. Hilaire, PhD, FAHA
University of Pittsburgh
BSTWR 1744.1
200 Lothrop Street, Pittsburgh, PA 15261
+1 412-648-9441 sthilair@pitt.edu

TOTAL WORD COUNT: 5062
ABSTRACT WORD COUNT: 301

Background: Calcific aortic valve disease (CAVD) is the pathological remodeling of the valve leaflets which leads to heart failure and high stroke risk. While several mechanisms are known to drive cardiovascular calcification, the initial steps orchestrating the osteogenic reprogramming of cells are not fully understood. Non-canonical functions of telomerase reverse transcriptase (TERT) include service as a cofactor to stimulate gene transcription, and TERT overexpression primes mesenchymal stem cells to differentiate into osteoblasts. We investigated whether TERT contributes to osteogenic reprogramming of valve interstitial cells.

Methods: Baseline transcription of TERT and osteogenic markers, senescence, DNA damage, and telomere length in valve tissue and primary aortic valve interstitial cells (VICs) from control and CAVD patients were assessed. TERT expression was depleted in cells using lentiviral vectors. Cells from *Tert*$^{+/+}$ and *Tert*$^{-/-}$ mice were used to validate human findings. Immunofluorescence staining, proximity ligation assay, and chromatin immunoprecipitation assay were used in mechanistic experiments.

Results: TERT protein was highly expressed in calcified valve leaflets, without changes in telomere length, DNA damage, or senescence. These phenotypic features were retained in primary VICs isolated and cultured from those diseased tissues. TERT levels were increased with osteogenic or inflammatory stimuli, and genetic deletion or reduction of *TERT* prevented calcification of VICs isolated from humans and mice. Similar results were seen in smooth muscle cells (SMCs) and mesenchymal stem cells (MSCs). TERT and Signal Transducer and Activator of Transcription 5A/B (STAT5) colocalize and bind to the Runt-Related Transcription Factor 2 (*RUNX2*) gene promoter, and TERT and STAT5 co-localized in calcified valve tissues. Pharmacological inhibition of STAT5A prevented calcification in vitro.

Conclusions: These data show that non-canonical TERT activity is required for the calcification of VICs. TERT partners with STAT5A to bind to and activate the *RUNX2* gene promoter. These data identify a novel therapeutic target to abate vascular calcification.

ABBREVIATIONS:

αSMA, alpha 2 smooth muscle actin; VICs, aortic valve interstitial cells; CAVD, calcific aortic valve disease; ChIP, chromatin immunoprecipitation; ECM, extracellular matrix; γ-H2AX, phosphorylated gamma histone 2AX; LPS, lipopolysaccharide; BMMSCs, bone marrow mesenchymal stem cells; MSCs, Mesenchymal stem cells; NT, no treatment; OPN, osteopontin; OST, osteogenic treatment; PCNA, proliferating cell nuclear antigen; RUNX2, runt-elated transcription factor 2; STAT5, signal Transducer and activator of transcription 5A/B; TERC, telomerase RNA component; TERT, telomerase reverse transcriptase catalytic subunit; TL, telomere length; αTUB, alpha Tubulin

Key Words:

aortic stenosis, vascular calcification, calcific aortic valve disease, osteogenic differentiation, TERT, STAT

Novelty and Significance

What Is Known?

- Calcific aortic valve disease (CAVD) is the most prevalent form of aortic valve pathology. CAVD strongly correlates with age and leads to heart failure and a high risk of stroke. Currently, the only therapeutic option is valve replacement, which comes with significant healthcare costs and additional risks to patients.
- Runt-related transcription factor 2 (RUNX2) is the master transcription factor required for osteogenic differentiation of osteoblasts and osteogenic reprogramming of vascular cells, yet the early events driving its transcription in valve cells are not well defined.
- Overexpression of TERT primes mesenchymal stem cells to differentiate down the osteoblast lineage, suggesting that TERT signaling plays an important role in cell differentiation and phenotype.

What New Information Does This Article Contribute?

- TERT protein is highly expressed in calcified aortic leaflets and valve interstitial cells, independent of changes in telomere length.
- Genetic loss or depletion of TERT blocks calcification in valve interstitial cells, coronary smooth muscle cells, and mesenchymal stem cells.
- TERT co-localizes with STAT5 in the cytosol and on the *RUNX2* gene promoter, the master regulator of osteogenic transcriptional programs.

98 • Pharmacological inhibition of STAT5 prevents calcification of human valve interstitial cells,
99 coronary smooth muscle cells, and mesenchymal stem cells.
100
101 *What are the clinical implications?*
102 • We have identified TERT/STAT5 as novel signaling axis that promotes the early
103 transcriptional reprogramming in cardiovascular cells. Inhibiting TERT and STAT5
104 interaction and activity can be leveraged for the development of pharmacological or
105 biological therapeutic strategies to halt or prevent calcification in the aortic valve and
106 perhaps other cardiovascular tissues.
107 • Surgical procedures are currently the only treatment option for patients with CAVD.
108 Discovering the early events driving vascular calcification identifies novel and druggable
109 targets for the development of non-surgical therapies.
110

111 **INTRODUCTION**

112 Calcific aortic valve disease (CAVD) encompasses a spectrum of pathological remodeling of the
113 valve leaflet, ranging from mild valve thickening that displays microcalcifications to
114 macrocalcifications that predominate in more advanced disease stages.[1] Aortic stenosis results
115 from fibrotic remodeling and the formation of calcified nodules on the valve leaflet that impede
116 and disrupt blood flow, causing excessive strain on the cardiac tissue, increasing the risk of
117 stroke, and leading to heart failure.[2] CAVD severity and incidence increase with age. CAVD
118 prevalence rapidly increases with age and is >1,000 per 100,000 individuals ≥75 years of
119 age.[3,4] Further, roughly 1-2% of the population harbors bicuspid aortic valve malformations, and
120 these malformed valves are prone to calcify and develop CAVD.[5] Currently there is no
121 therapeutic treatment that halts or reverses pathologic calcification that occurs in the valve
122 leaflets, or other cardiovascular tissues. The only therapeutic option to treat aortic stenosis is
123 valve replacement via surgical or transcatheter procedures, incurring substantial medical costs
124 and health care burden to the patient.[6]

125

126 Aortic valve interstitial cells (VICs) are the primary cell type of the valve leaflet and are
127 responsible for maintaining valvular integrity. VICs reside in a quiescent state; however,
128 adaptive or maladaptive responses to environmental factors such as inflammation, breakdown
129 of the extracellular matrix (ECM), and mechanical stress may disrupt VIC homeostasis.[7,8] With
130 alterations in homeostasis, VICs acquire a myofibroblast-like phenotype, termed “activated
131 VICs,” capable of proliferation, contraction, and secretion of proteins that further remodel the
132 extracellular milieu.[9] Activated VICs can transition into a calcifying cell; however, how the initial
133 steps regulating the osteogenic switching of cells are not fully understood. It is well established
134 that the osteogenic differentiation of VICs and also vascular smooth muscle cells (SMCs) is

135 similar to the differentiation of mesenchymal stem cells (MSCs) into bone-forming osteoblasts;
136 osteogenic differentiation is primarily orchestrated by Runt-related transcription factor 2
137 (*RUNX2*), the master transcriptional regulator of osteogenic transcriptional programs.[10-12] Other
138 osteogenic signature markers such as osteocalcin, alkaline phosphatase, and osteopontin are
139 also upregulated in calcifying stem and valvular cells.[9,13] While it is accepted that VICs
140 upregulate the expression of osteogenic genes in response to stresses such as inflammation,
141 extracellular matrix (EMC) remodeling, and mechanical stress, the causal relationship between
142 those stresses and the initial events in the activation of osteogenic transcriptional
143 reprogramming remains ill-defined.
144
145 The telomerase complex consists of the telomerase RNA component (TERC) and telomerase
146 reverse transcriptase (TERT) protein, and functions to maintain chromosome telomere length
147 and genome integrity.[14] Independent of telomerase activity, TERT also exhibits non-canonical
148 functions. TERT can regulate gene expression and help orchestrate chromatin remodeling.[15-17]
149 For example, TERT acts as a cofactor in Wnt-dependent promoter activation by interacting with
150 the chromatin remodeling protein Brahma-related gene 1 (BRG1), facilitating the expression of
151 Wnt/β-catenin target genes.[18] In a murine model of atherosclerosis TERT induced chromatin
152 remodeling and SMC proliferation by chaperoning the retinoblastoma-associated transcription
153 factor 1 (E2F1) binding to S-phase gene promoters.[19,20] Linking together the themes of
154 calcification and non-canonical TERT, two contemporary studies identified that the
155 overexpression of *TERT* primed human MSCs to differentiate down the osteogenic lineage and
156 develop bone-like structures.[21,22] The mechanism by which TERT drives the osteogenic
157 differentiation of human MSCs is unknown. Collectively, these studies provide strong evidence
158 of telomerase-independent functions of TERT in altering chromatin states and regulating gene
159 expression via various protein-protein interactions.

160

161 In this study, we tested the hypothesis that TERT contributes to the osteogenic transition of
162 VICs. We utilized primary human aortic valve tissues from healthy control donors and CAVD
163 patients and generated patient-specific VIC lines for in vitro disease modeling. We established
164 baseline patterns and osteogenic induction of *TERT* and calcification markers in CAVD tissue
165 and VICs, and assessed the consequences of genetic deletion or depletion of *TERT* during
166 osteogenic differentiation in several cell types. We further defined the underlying mechanism by
167 which TERT and STAT5 participate in the osteogenic transition of VICs.

168 **METHODS**

169 **Data Availability**

170 The Materials and Methods and the Major Resources Table are available in the Supplemental
171 Material. The data that support the findings of this study, experimental materials, and analytic
172 methods are available from the corresponding author upon reasonable request.

173 **RESULTS**

174 **TERT is upregulated in CAVD valve tissue**

175 Human aortic valves were collected after surgical aortic valve replacement procedures or from
176 cadaveric tissue obtained via the Center for Organ Recovery and Education (CORE) of the
177 University of Pittsburgh and processed as previously described.[23] Macroscopic examination and
178 histological staining with Von Kossa were used to determine and confirm whether valves could
179 be classified as a non-calcified control or as having calcific aortic valve disease (CAVD) (**Figure**
180 **1A, Supplemental Figure 1A, Table 1 and 2: Patient Information**). RUNX2 is the master
181 transcription factor required for stem cells to differentiate into osteoblasts,[24] and is critical for the
182 pathological osteogenic differentiation of vascular cells.[25] Immunofluorescent staining of the
183 early calcification marker RUNX2 and the late calcification marker OPN show they were

184 significantly upregulated in CAVD tissue compared to control tissues, indicating activation of
185 osteogenic transcriptional programs in CAVD tissues (**Supplemental Figure 1B**). As TERT is
186 highly expressed in stem cells and its overexpression primes MSCs to differentiate into the
187 osteogenic lineage,[21,22] we analyzed the expression of the *TERT* transcript and found that it was
188 significantly upregulated in CAVD tissue relative to control samples (**Figure 1B**), and its levels
189 positively trend with the donor's age (**Supplemental Figure 1C**). The expression of genes
190 involved in senescence (Cyclin Dependent Kinase Inhibitor 1A (*CDKN1A*) and Galactosidase
191 Beta 1 (*GLB1*)), proliferation (Proliferating Cell Nuclear Antigen (*PCNA*)), DNA damage (Tumor
192 Protein 53 (*TP53*)), and cytoskeletal markers (actin Alpha 2 Smooth Muscle/αSMA (*ACTA2*);
193 Vimentin (*VIM*)) and interleukin 6 (*IL6*) showed no differences, while the inflammatory marker
194 and tumor necrosis factor alpha (*TNF)* was elevated in CAVD samples (**Supplemental Figure**
195 **1D**), suggesting a role for inflammatory signaling in calcification pathogenesis, as also observed
196 by others.[26,27]
197
198 TERT protein expression and distribution was analyzed in serial sections of control and CAVD
199 tissues. We detected an elevated TERT protein signal in CAVD valves compared to controls,
200 with the signal localized to areas of calcification, and the number of cells expressing TERT was
201 significantly elevated in CAVD tissues compared to non-calcified control tissues (**Figure 1C**).
202 TERT was observed in both nuclear and cytosolic areas (**Supplemental Figure 1E).** No
203 differences were detected in the staining levels of proliferation marker proliferating cell nuclear
204 antigen (PCNA) or the DNA damage indicator phosphorylated gamma histone 2AX (γ-H2AX),
205 between CAVD and control tissues (**Supplemental Figure 1F**). We found no differences in
206 relative mean telomere length between control and CAVD tissues (**Figure 1D**), indicating similar
207 canonical telomere extending functions of TERT in both groups. The mean age of CAVD and
208 control patients in this study was 68 and 54 years old, respectively (**Figure 1E**). Together, these

209 data show that TERT, osteogenic markers, and inflammatory signatures are upregulated in
210 CAVD tissue while markers indicating alterations in proliferation, DNA damage, and senescence
211 are not altered in CAVD leaflets. Importantly, despite the elevated TERT expression and protein
212 levels, telomere length remains unaltered between CAVD and control tissue, suggesting non-
213 canonical TERT activity.
214
215 **CAVD in vitro disease modeling with VICs recapitulates in vivo observations**
216 We created patient-specific VIC lines isolated from CAVD and control valves.[23] At baseline,
217 VICs freshly isolated from CAVD and control patients exhibited no morphological, proliferative,
218 or migratory differences (**Figures 2A, 2B**, **2C**, **and Supplemental Figure 2A,** respectively)
219 while TERT and RUNX2 proteins were significantly elevated in CAVD VICs (**Figure 2D**). At
220 baseline, we observed no differences between CAVD and control VICs in SM22 or αSMA —
221 markers of an activated VIC phenotype (**Supplemental Figure 2B**)— but found significantly
222 higher levels of the mineralizing enzyme tissue non-specific alkaline phosphatase (TNAP) in
223 CAVD VICs (**Supplemental Figure 2C**). Like in the leaflet, there was no difference in the mean
224 telomere length between CAVD and control groups (**Figure 2E**). Thus, these data show that at
225 baseline, VIC isolated from CAVD patients display elevated TERT and RUNX2 expression,
226 recapitulating the osteogenic phenotype observed in CAVD leaflet tissue, and confirming the
227 telomere activity of TERT is not operative in these established cells lines.
228
229 **TERT expression is upregulated in VICs under osteogenic conditions**
230 To model CAVD disease in vitro and establish a role for TERT during VIC osteogenesis, we
231 cultured CAVD and control VICs in osteogenic media conditions (OST, see Methods Section), a
232 media widely utilized to induce osteogenic differentiation of osteoblasts.[28] Calcification was
233 visualized using Alizarin Red stain and revealed that OST-treated CAVD and control VICs lay

down calcified matrix as early as 14 days (d14), and CAVD VICs calcified earlier relative to control VICs under the same conditions. Importantly, we observed that CAVD VICs calcify de novo under no treatment (NT) conditions, suggesting that CAVD VICs are primed for osteogenesis (**Figure 3A**). Protein analysis revealed increased levels of TERT in control VICs at d14 of OST treatment, while in CAVD VICs TERT was elevated under NT conditions, suggesting that TERT has an active role in the osteogenesis of VICs. The calcification markers RUNX2 and OPN were upregulated indicating active osteogenesis (**Figure 3B**). Immunofluorescent staining of VICs showed that at d14 under NT conditions, TERT was elevated in CAVD VICs relative to control VICs (**Figure 3C**, left panels) and that TERT signal was intensified on d14 of OST treatment (**Figure 3C**, right panels). While both control and CAVD VICs exhibit calcification on d14, CAVD VICs form larger calcified nodules (**Figure 3C**, right panels), and we observed no differences in cell numbers at the end of the 14-day assay under NT or OST treatment conditions (**Supplemental Figure 3A**). Transcriptional analysis showed that the osteogenic markers *BMP2*, *THBS1*, *ALPL;* myofibroblast markers *CNN1*, *TAGLN*, *SMTN;* calcification-associated gene *FOXO1;*[29] and the CAVD-associated metalloproteinase *MMP13*[30] were significantly upregulated in control VICs at d14 of OST treatment. We also found significant upregulation of the pro-inflammatory transcription factor Signal Transducer and Activator of Transcription 5A *(STAT5A)* gene while the expression of the isoform *STAT5B* gene remained unchanged (**Figure 3D**). These results confirmed that VICs undergo osteogenesis as opposed to de novo mineral nucleation.[31]

In cancer and stem cells, the enhanced canonical activity of TERT leads to long telomeres and enables unlimited proliferation,[32] while short telomeres can trigger cellular senescence.[33] Although we observed no differences in telomere length (**Figure 1D and 2E**), we assessed cellular senescence. We observed no differences in the expression of senescence-associated

259 β-galactosidase (SA-β-gal, *BGLAP*) between CAVD and control VICs at baseline
260 **(Supplemental Figure 3B)**, or during osteogenic treatment (**Figure 4D**). We further assessed
261 cellular senescence by senescence-associated β-galactosidase activity assay. We found that
262 the osteogenic treatment did not trigger cellular senescence even after 28 days (**Supplemental**
263 **Figure 3C**). These data confirmed that cellular senescence is not operative during the VIC
264 osteogenesis.
265
266 **TERT is required for in vitro calcification**
267 Previous studies have shown that the overexpression of TERT primes human MSCs (hMSCs)
268 to differentiate into osteoblasts.[21,22] To determine whether TERT is required for the calcification
269 of human VICs, we transduced these VICs with a lentivirus expressing an shRNA targeting
270 *TERT*. Knockdown of *TERT* caused inhibition in the calcification of VICs relative to VICs
271 transduced with a scramble shRNA control, and downregulation of RUNX2 in human VICs
272 (**Figures 4A and 4B**). Next, we assessed whether inhibition of the canonical telomere extending
273 activity of TERT altered calcification of VICs. Cells under OST treatment were given the inhibitor
274 BIBR1532, which blocks the reverse transcriptase activity of TERT, required for telomere
275 extension.[34] A 28-day OST assay treatment with BIBR1532 did not alter the calcification of VICs
276 (**Figure 4C**), suggesting that the canonical telomere-extending function of TERT is not required
277 during VIC osteogenesis. Next, we assessed whether TERT was involved in the osteogenic
278 reprogramming of other cell types. In human coronary artery smooth muscle cells (CASMCs),
279 knockdown of TERT also inhibited calcification (**Figure 4D**). To validate these findings and
280 confirm a broader role for TERT in osteogenic differentiation, we investigated TERT's effect in
281 human MSCs. Human MSCs exhibited robust calcification as early as day 14 of the OST
282 treatment, while cells in NT conditions did not calcify (**Supplemental Figure 4A**). Protein
283 analysis showed TERT protein level increases on day 3 of the OST differentiation, coinciding

284 with the increase in *RUNX2* expression and RUNX2 protein levels (**Supplemental Figures 4B**
285 **and 4C**). Like human VICs, human MSCs in OST treatment exhibited intense TERT staining,
286 and TERT-positive cells clustered around calcified nodules (**Supplemental Figure 4D**). As in
287 our previous assays, the knockdown of *TERT* inhibited calcification of human MSCs
288 (**Supplemental Figures 4E and 4F**). Together, these data suggest that TERT is required for
289 the osteogenic differentiation of human VICs, CASMCs, and MSCs.
290
291 To further confirm our findings that TERT is required for calcification, we utilized a genetic
292 approach. Murine VICs (mVICs) and bone marrow MSCs (mBMMSCs) were isolated and
293 expanded from *Tert*-knockout (*Tert*$^{-/-}$) and wild-type (*Tert*$^{+/+}$) mice.[35] *Tert*$^{-/-}$ mice were generated
294 from heterozygous breeding pairs (F1 generation) and thus do not exhibit shortened
295 telomeres.[36] In support of our findings in the human cells with depletion of *TERT*, we found that
296 deletion of *Tert* drastically inhibited calcification of mVICs and mBMMSCs compared to *Tert*$^{+/+}$
297 cells, which exhibited robust calcification, as revealed at d21 of OST treatment by Alizarin Red
298 staining (**Figures 5A and 5B**). Notably, TERT deficiency or OST treatment did not induce
299 senescence in mice *Tert*$^{-/-}$ cells as determined by SA-β-gal activity (**Supplemental Figures 5A**
300 and **5B**). Together, these data show that TERT is required for the osteogenic transition of mice
301 VICs and BMMSCs, and that senescence is not operative during the osteogenic differentiation
302 of murine cells.
303
304 **TERT Interacts with STAT5 to bind the *RUNX2* gene promoter**
305 TERT exerts transcriptional gene regulation in various tissues and cells by physically interacting
306 with transcription factors such as NF-κB, Sp1, and E2F1.[17,20,37,38] Increased RUNX2 expression
307 and activity is the hallmark of osteoblast differentiation and vascular calcification.[25] RUNX2 is
308 the master regulator of osteogenic differentiation and we found that RUNX2 is downregulated in

309 *TERT*-knockdown cells (**Figure 4**). We used the LASAGNA[39] and TRANSFAC/MATCH[40]
310 programs to identify putative transcription factor binding sites in the 5kb region upstream of the
311 human *RUNX2* gene promoter (NM_001015051.3) and identified 13 potential STAT5 binding
312 sites (**Table 2**). We observed increased expression of *STAT5A* during the osteogenic
313 differentiation of VICs (**Figure 3D**). Two different genes encode STAT5A and STAT5B, but 96%
314 of their amino acid sequence is shared and their activities redundant; herein we refer to both
315 genes as STAT5 when available tools (e.g. antibodies) do not allow for isoform differentiation.[41]
316 We found that OST treatment upregulated STAT5 protein in VICs, and STAT5 was detected in
317 the nucleus of OST-stimulated VICs (**Supplemental Figures 6A and 6B**). Next, we utilized
318 proximity ligation (PLA) to examine TERT and STAT5 colocalization, as this technique is
319 capable to detect interacting proteins in a proximity range below 40 nm. PLA revealed that
320 TERT and STAT5 significantly colocalized in control VICs after 21 days of OST treatment
321 (**Supplemental Figure 6C**). Likewise, TERT/STAT5 colocalization was elevated in CAVD VICs
322 after 21 days of OST treatment compared to control VICs (**Figure 6A**). We next sought to
323 determine whether TERT and STAT5 are bound to the *RUNX2* gene promoter region. We
324 identified 13 potential STAT5 binding sites (**Table 2**) and focused on sites -1371 bp and -193 bp
325 upstream of the start site as both have high homology to the tetrameric consensus STAT5
326 binding site and show an elevated likelihood of being functional sites (core and matrix scores of
327 0.788 and 0.834, and 0.995 and 0.882, respectively, **Figure 6B**). Chromatin
328 immunoprecipitation analysis (ChIP) in control VICs shows that STAT5 binds to the *RUNX2*
329 promoter at both sites, and that the binding enrichment was significantly higher during
330 osteogenic differentiation (**Figure 6C**). While we found that TERT also binds to -1371 bp and -
331 193 bp of RUNX2 promoter, the trending enrichment during OST treatment did not reach
332 statistical significance, perhaps suggesting that TERT itself does not bind to DNA directly but
333 sits alongside STAT5 on the *RUNX2* gene promoter.

334

335 We utilized a pharmacological approach to identify whether one or both STAT5 proteins
336 contribute to osteogenic reprogramming. We treated human VICs with the small molecules
337 StafiA-1 and StafiB-1, which have been reported to specifically inhibit STAT5A and STAT5B,
338 respectively.[42,43] We found that StafiA-1 significantly inhibited calcification of VICs during a 21
339 days OST assay and that this inhibition was of a greater extent than the inhibition observed
340 when VICs were treated with StafiB-1, suggesting that STAT5A is the main participant during
341 the osteogenic reprogramming of VICs (**Figure 6D**). Similarly, we found that StafiA-1
342 significantly reduced the calcification in human CASMCs and MSCs while StafiaB-1 did not
343 (**Supplementary Figures 6D and 6E**). Together, these data show that TERT and STAT5A
344 interact to localize STAT5A to its cognate sites in the *RUNX2* promoter to drive osteogenic
345 transcriptional reprogramming.

346

347 We explored the mechanism by which TERT and STAT5 become activated during the
348 osteogenic differentiation of human VICs. As inflammation contributes to CAVD pathogenesis,[44]
349 we used bacterial lipopolysaccharide (LPS) to trigger inflammatory response pathways in VICs[45]
350 and found that LPS was sufficient to induce calcification of VICs. Like OST treatment, TERT-
351 positive cells accumulated near calcified nodules after LPS and osteogenic stimulation
352 (**Supplementary Figure 6F**). Protein analysis showed that LPS alone was also sufficient to
353 upregulate TERT, RUNX2, and STAT5 proteins (**Supplementary Figure 6G**). Together, these
354 observations indicate that LPS/TLR4 inflammatory signaling pathway participates in the
355 regulation of TERT and the osteogenic transition of human VICs.

356

357 **TERT and STAT5 are upregulated in CAVD tissue**

358 Our data illustrate a requirement of TERT for calcification and show TERT/STAT5A drives
359 osteogenic reprogramming by binding to the *RUNX2* gene promoter. To confirm the role of
360 these proteins in vivo, we quantified the staining of TERT and STAT5 in human valves. We
361 found that STAT5 protein is highly expressed in the CAVD leaflet and localized to areas of
362 calcification, mirroring TERT distribution in the valve leaflet, while the number of STAT5-positive
363 cells was significantly increased in CAVD tissue (**Figure 7A**). Furthermore, STAT5 highly
364 colocalized to TERT-positive cells in the valve (**Figure 7B**). Altogether, these data support our
365 in vitro investigations and suggest that TERT contributes to CAVD pathogenesis via its
366 interaction with STAT5A.
367

368 **DISCUSSION**

369 This study reveals a novel mechanism for TERT in driving a human pathology (**Figure 8**). These
370 data establish that TERT is upregulated in CAVD tissue and in primary cell lines derived from
371 those tissues, and that TERT is required for the osteogenic transition of vascular cells. The
372 mechanism by which TERT promotes the osteogenic reprogramming of VICs is via interaction
373 with STAT5, and this complex binds to the *RUNX2* gene promoter. Depletion of TERT or
374 pharmacological inhibition of STAT5 blocked calcification in vitro, and TERT/STAT5 puncta
375 were observed on CAVD but not control human aortic valves. Collectively, these experiments
376 support a novel role for TERT and STAT5 in driving CAVD pathogenesis and identify a unique,
377 druggable target for cardiovascular calcification.
378

379 TERT is well-known for its canonical, telomere-extending activity, yet TERT also regulates gene
380 expression and chromatin remodeling independent of affecting telomere integrity. For example,
381 previous reports have shown that TERT interacts physically with several transcription factors to

382 promote the expression of several genes, including β-catenin to stimulate genes involved in
383 bone development.[15,16,37] In the vasculature, TERT binds to the transcription factors SP1 at the
384 *VEGF* promoter and E2F1 at *MCM7*, *CCNA1*, and *PCNA* promoters, stimulating SMC
385 proliferation and neointima formation.[20,35,38,46] In this regard, we did not detect proliferative or
386 migratory differences between control and CAVD VICs despite elevated levels of TERT at
387 baseline (**Figures 2B and 2C**).
388
389 In addition to supporting transcription factor function, TERT also acts as a cofactor to
390 orchestrate chromatin remodeling machinery. TERT serves as a chaperone to facilitate the
391 recruitment of BRG1 and histone acetyltransferases to stimulate chromatin accessibility and
392 transcription or to maintain heterochromatin structure.[18,47,48] Loss of TERT abrogates the cellular
393 response to DNA double-strand breaks and alters the overall chromatin configuration, without
394 affecting the short-term telomere integrity.[17] These data strongly support the prominent role of
395 non-canonical functions of TERT. We found that TERT interacts with STAT5 and together, are
396 recruited to two consensus sites in the *RUNX2* gene promoter during osteogenic
397 reprogramming of VICs. Our observations that TERT is upregulated in CAVD tissue and during
398 VIC osteogenesis support this hypothesis. Furthermore, our findings that *TERT* depletion
399 reduced RUNX2 expression and calcification in several cell types, along with the finding of
400 others that *TERT* overexpression drives osteogenesis in human MSC,[21,22] support a general
401 role for TERT modulating cellular phenotypic transition and osteogenic reprogramming. From
402 the studies mentioned above, one can speculate that perhaps TERT serves as a co-factor
403 bridging chromatin remodeling complexes and transcription factors to facilitate euchromatin
404 stability.
405

406 Cell replication progressively shortens telomeres, triggering senescence, yet telomere length
407 varies widely between people of the same age.[49] Telomere length is considered a biomarker of
408 aging, and several studies have utilized circulating leukocytes to investigate whether shortened
409 telomeres correlate with various vascular disease states.[50,51] One study correlated circulating
410 leukocytes as surrogates to interrogate the telomere length of patients diagnosed with CAVD
411 featuring aortic stenosis and found that CAVD leukocytes had slightly shorter telomeres than
412 age-matched healthy controls.[52] However, telomere length in leukocytes is not indicative of
413 global telomere length, telomerase complex activity, or TERT protein function in all cell types.
414 First, short telomeres may reflect increased circulating leukocyte turnover due to systemic
415 inflammation, as leukocytes are highly proliferative. Second, telomere attrition might be a tissue-
416 and disease-dependent process. Third, these correlative studies show no clear evidence of a
417 causal link between telomere length, non-canonical TERT activity, and disease progression. In
418 this regard, Huzen et al. compared the telomere length of the leukocytes of age-matched
419 healthy controls and patients with atherosclerosis as well as the telomere length of the cells in
420 the atherosclerotic plaques of the patients. They found that while telomere length in leukocytes
421 from the atherosclerosis patient group was significantly shorter than in the control group,
422 telomere length in the atherosclerotic plaques was significantly longer, indicative of increased
423 telomerase activity.[53] Thus, total leukocyte telomere length does not represent telomere length
424 in the diseased tissue itself. Our approach examined TERT protein expression directly in the
425 valve tissue and in patient-specific VICs. With these tools, we determined that the expression
426 levels of TERT and osteogenic markers in CAVD tissue were elevated, without changes in
427 telomere length, proliferation, and DNA damage markers; thus, suggesting a non-canonical role
428 for TERT in these cells.
429

430 VIC calcification shares aspects of the transcriptional program observed during the
431 differentiation of MSCs into osteoblasts, including the upregulation of *RUNX2, BGLAP, TNAP*,
432 and the secretion of bone-forming proteins and accumulation of calcium minerals.[5,10,12] Likewise,
433 mechanical stress, disturbed flow, and inflammation promote VIC calcification, as well as the
434 osteogenic differentiation of MSCs.[54] These observations suggest that VICs switch from their
435 quiescent state and undergo an osteogenic transition like MSCs, acquiring osteoblast-like
436 phenotypic features. The mechanisms driving these cell transitions are not fully understood. We
437 have hypothesized that fully differentiated cells can de-differentiate into a transitory, multipotent
438 stem cell-like state and then acquire an osteogenic phenotype.[55] VICs have the potential to
439 differentiate into the osteogenic, chondrogenic, or adipogenic lineage, properties comparable to
440 mesenchymal stem cells.[56] We focused on TERT as it is highly expressed in stem cells and its
441 overexpression primes mesenchymal stem cells into the osteogenic lineage.[21,22] Thus, we
442 propose that the upregulation of TERT leads healthy VICs to undergo a de-differentiation
443 process, likely to involve broad chromatin remodeling and that in an inflammatory milieu, TERT
444 and STAT5A couple to drive the osteogenic transition of VICs.
445
446 The osteogenic differentiation of stem cells is orchestrated by RUNX2, which is also detected in
447 the osteogenic reprogramming of vascular cells.[25,57] In a recent transcriptomic study Xu et al.
448 identified 14 cell populations present in aortic valve tissue samples from two healthy and four
449 CAVD valves.[58] CAVD was diagnosed via ultrasound imaging, which detects leaflet mobility,
450 however examining the macroscopic pictures and histological staining of valve leaflets used in
451 this analysis shows that while these valves are indeed stiff, they do not exhibit robust nodules of
452 calcification as do the valves in our data set (**Figures 1A, 1C, 5, and Supplemental Figure**
453 **1A**). Their analysis identified three VIC populations defined by expression of *FOS, HSPA6,*
454 *SPARC.* However, cells from six valves were pooled, with 10.4% of cells coming from control

455 tissue and the remaining 89.6% from CAVD tissues. Bulk transcriptomic data from these tissues
456 show only a small 1.49-fold increase in *RUNX2* gene expression in CAVD tissues, in stark
457 contrast with our observations regarding RUNX2 expression (**Figures 1-3**) and what is currently
458 accepted.[10-12] Inspection of the publicly available bulk RNA-sequencing data (PRJNA552159)
459 did not show any increase in *TERT* transcript expression. While hemodynamic data showed
460 those valves had indeed undergone fibrotic remodeling, only a low number of calcifying cells
461 were present, as confirmed by their histological staining. This lack of calcification may explain
462 why *TERT* expression was undetected in their study. In our study, a portion of each patient
463 valve was used for cell isolation while the rest was utilized for calcification assessment by
464 histological staining, following a workflow that we developed that guarantee that cells isolated
465 from surgically removed and postmortem tissues retain their proliferative capacity and
466 endothelial and interstitial phenotypes in culture.[23]
467
468 The function of STAT5 in bone formation is multifaceted. While it was shown that STAT5 can
469 promote the differentiation of MSCs into osteoblasts by upregulation of the osteogenic genes in
470 a Jak2-dependent manner,[59] a *Stat5a* global knockout mouse exhibited elevated bone mass
471 and bone mineral density.[60] These conflicting reports indicate that the role of STAT5 in bone
472 formation and remodeling is complex and more studies are required. STAT5 has diverse
473 functions as a transcription factor: it interacts with histone acetyltransferases and transcription
474 factors such as the glucocorticoid receptor, SP1, YY1, and C/EBPβ to stimulate gene
475 expression,[61-63] and two studies in cancer cells identified that STAT5 induces *TERT*
476 expression.[64,65] We found multiple putative STAT5 binding sites in the *RUNX2* promoter region
477 and provide strong evidence in support of a novel mechanism in CAVD pathogenesis where
478 TERT/STAT5 co-localize, translocate to the nucleus, and activate osteogenic gene transcription
479 which drives the early events in cellular osteogenic transition.

While our results are robust, it is important to address the limitations of our study. STAT5A and STAT5B are two different genes with 96% of their amino acid sequence shared and their activities redundant.[41] We have determined that VICs express both variants, however, our antibodies could not differentiate between the two variants, thus it is possible that only one isoform interacts with TERT to bind the *RUNX2* gene promoter. STAT5 is activated by multiple cytokines, including IL-2, IL-6, and TNF-α,[66] and it was shown that IL-2 specifically activates STAT5 to induce TERT expression in cancer cells.[64] Whether STAT5 first induces TERT expression, and then TERT and STAT5 together cooperate to control the expression of RUNX2 needs to be determined. There is also redundancy regarding STAT1/3/5 functions and signaling.[67] Our study was not designed to address all the complexities of STAT signaling per se but rather to investigate the role of TERT utilizing STAT5 as a DNA transcription factor binding partner to activate an osteogenic transcriptional program; our future studies will investigate the role of STAT5 further.

Our work highlights the importance of primary human tissue-based studies. Murine models are not ideal to study non-genetic drivers of CAVD, as mice do not develop CAVD de novo.[68,69] Mouse leaflets' structure differs from human leaflets as they lack a trilaminar organization and present a melanocyte cell population.[70-72] Recent elegant work from the Giachelli group showed that in mice, calcification happens in the sinus wall and to a lesser extent, at the leaflet hinge, the region between the leaflet VICs and SMCs of the aorta, with no detectable calcification in the leaflets after 26 weeks of a high-fat diet in a *LDLR* knockout mice model.[73] This distribution is similar to the atherosclerotic calcification observed of the aortic root, and it is also found in a work from the Kobuta group, which detected calcification in the sinus wall after 16 weeks of valve mechanical injury.[68] Therefore, mice models do not fully recapitulate calcification or

505 pathogenesis of CAVD in humans in terms of leaflet remodeling and calcification; as such,
506 murine-based studies may not be ideal models for studying human valve disease, positioning
507 human-based studies as imperative to understand and solve the pathologic calcification of the
508 valve tissue.
509
510 We have identified a novel and innovative mechanism that contributes to CAVD pathogenesis
511 by determining a causal link between TERT and the osteogenic differentiation of valve cells.
512 This study is the first to suggest that a non-canonical function of TERT is operative in CAVD
513 pathogenesis as we did not detect telomere length differences in our specimens and the cell
514 lines established out of them. TERT was detected in the cytosol and nuclei of cells, its
515 expression was required for calcification of several cell systems, and we detected TERT bound
516 to the *RUNX2* promoter region, dynamically changing its binding during osteogenic
517 differentiation of VICs, suggesting an active non-canonical role as a STAT5-binding partner.
518 Current CAVD therapies are surgical, limited to either mechanical or bioprosthetic valve
519 replacement, and performed only when the disease has progressed to the advanced point of
520 affecting blood flow and heart function. As TERT and STAT5 become important targets in
521 cancer therapy, we propose these novel targets may perhaps be leveraged to tackle
522 calcification disease progression. Studying the disease mechanisms and effects of TERT and
523 STAT5 interaction in the context of maladaptive dysregulation in the vessels could also better
524 inform us of potential drugs to disrupt their interaction and prevent, or even reverse CAVD.
525
526 **ACKNOWLEDGEMENTS**
527 We would like to acknowledge and thank the Center for Organ Research and Education for their
528 help and support and thank tissue donors and their families for making this study possible. We
529 would also like to thank Kristin Konopka, tissue bank coordinator at The Department of

530 Cardiothoracic Surgery, UPMC. We would like to thank Jason Dobbins for his insightful
531 discussion and critical reading of this manuscript.
532
533 **SOURCES OF FUNDING**
534 This study was supported by funds from the National Institutes of Health (R01 HL142932, St.
535 Hilaire) and the American Heart Association (20IPA35260111, St. Hilaire; 902641, Cuevas).
536
537 **DISCLOSURES**
538 The University of Pittsburgh has filed a provisional patent application on behalf of CSH and RAC
539 regarding technology based on findings presented in this manuscript. IS receives institutional
540 research support from Atricure and Medtronic and serves as a consultant for Medtronic
541 Vascular. None of these conflicts of interest are related to this work. All other authors have
542 nothing to disclose.
543
544 **FIGURE LEGENDS**
545 **Figure 1. TERT is upregulated in CAVD valve tissue.**
546 A, Surgically removed specimen of control (top) and CAVD (bottom) human valves. B, TERT
547 mRNA transcript quantification in control and CAVD valve tissues. n = 8 control, n= 9 CAVD. C,
548 Representative serial sections of Von Kossa (dark precipitation, top panels) and TERT
549 immunofluorescent staining (bottom panels) in control and CAVD valve tissues. Scalebar 100
550 µm. Quantification of TERT intensity and the number of TERT-positive cells on the leaflet is
551 shown on the right graphs. n = 9 control, n = 9 CAVD. D, Telomere length measurements in
552 valve tissues. n = 16 control, n = 10 CAVD. E. Age of the patients utilized in this study. n = 25
553 control, n = 16 CAVD. Data are shown as means ± SD. *P* values were calculated by the Mann-
554 Whitney *U* test and shown on each graph.

555

556 **Figure 2. Valve interstitial cells isolated from CAVD patients show elevated TERT**

557 **expression at baseline.**

558 A, Representative images showing cell morphology of control (left) and CAVD (right) VICs.

559 Scalebar 50 µm. B, Proliferation of control and CAVD VICs at baseline. n = 3 control, n = 3

560 CAVD. Data represents means ± SD. C, Relative migration distances of control and CAVD

561 VICs. n = 10 control, n = 10 CAVD. Representative western blot staining of control and CAVD

562 VICs at baseline. Quantification of protein levels is shown on the right panels. n = 4 control, n =

563 4 CAVD/. E, Telomere length measurements in VICs. n = 8, control, n = 5 CAVD; means ± SD.

564 Data are shown as means ± SD. *P* values were calculated by the Mann-Whitney *U* test and

565 shown on each graph.

566

567 **Figure 3. TERT is upregulated during osteogenic differentiation of VICs.**

568 A, Representative images of VICs growing in normal conditions (no treatment, NT, left panel) or

569 stimulated with osteogenic media (OST) for 14 days. Calcium deposition was visualized by

570 Alizarin Red staining. Scalebar 50 µm. Quantification of calcification is shown as average

571 absorbance ± SD on the right graphs. n = 7 control, n = 7 CAVD. B, Representative western blot

572 staining of samples from control and CAVD VICs after 14 days of NT or OST. Quantification of

573 protein levels is shown on the right graphs. n = 4 control, n = 4 CAVD. C, Representative

574 immunofluorescent staining images of TERT in control and CAVD VICs after 14 days of NT or

575 OST. Calcium deposition was visualized by OsteoImage staining. Scalebar 100 µm. D.

576 Expression profile control VICs after 14 days of NT and OST treatment. n = 4 NT, n = 4 OST.

577 Data are shown as means ± SD. *P* values were calculated by the Mann-Whitney *U* test with * *P*

578 = 0.0286 in Figure D.

579

580 **Figure 4. TERT is required for osteogenic transition and calcification of human cells.**
581 A, VICs transduced with lentivirus containing either short hairpin scramble (shControl-GFP) or
582 short hairpin TERT (shTERT-GFP) and followed by OST stimulated for up to 28 days. Calcium
583 deposition was visualized by Alizarin Red staining. Quantification of calcification is presented as
584 average absorbance on the right graph. n = 6 shControl, n = 6 shTERT at 21 days and n = 9
585 shControl, n = 9 shTERT at day 28. Scalebar 400 µm. Data are shown as means ± SD. B,
586 Representative western blot staining of VICs transduced with lentivirus containing either
587 shControl-GFP or shTERT-GFP followed by 7 days of osteogenic stimulation. C. VICs treated
588 with BIBR1532 and stimulated with osteogenic media for 28 days. Scalebar 50 µm.
589 Quantification of calcification is shown on the right graph. n = 6. Data are shown as means ±
590 SD. D, CASMCs transduced with lentivirus containing either shControl-GFP or shTERT-GFP
591 and stimulated with osteogenic media for up to 21 days. n = 4 shControl, n = 4 shTERT for both
592 time points. Scalebar 400 µm. Quantification of calcification is shown on the right graph. *P*
593 values were calculated with the Kruskal-Wallis *H* test with Dunn post hoc test and shown on top
594 of each graph.
595
596 **Figure 5. TERT is required for the osteogenic transition of murine cells.**
597 A, Representative images of mVICs isolated from wild-type ($Tert^{+/+}$) or F1 Tert knockout ($Tert^{-/-}$)
598 mice and stimulated with osteogenic media for 21 days. Scalebar 100 µm. Quantification of
599 calcification is shown on the right graph. B, Representative images of mBMMSCs isolated from
600 $Tert^{+/+}$ or $Tert^{-/-}$ mice and stimulated with osteogenic media for 21 days. Scalebar 100 µm.
601 Quantification of calcification is presented as average absorbance on the right graphs. All
602 graphs are n = 4 $Tert^{+/+}$, n = 4 $Tert^{-/-}$. Data are shown as means ± SD. *P* values were
603 calculated by the Mann-Whitney U test and indicated on each graph.
604

605 **Figure 6. TERT and STAT5 interact to upregulate RUNX2 expression in human VICs.**

606 A, Diagram of proximity ligation assay (PLA, left panel). Representative images of TERT/STAT5
607 complex (red foci) in CAVD VICs cultured for 21 days in osteogenic medium and detected by
608 PLA. Scalebar 100 µm (middle panel). Quantification of PLA signal is shown in the right graph.
609 n = 4. B, Logo analysis depicting the consensus binding site for tetrameric STAT5 (top panel).
610 Diagram depicting STAT5 and TERT binding RUNX2 promoter and the positions of the
611 predictedSTAT5 binding sites (bottom panel). C, STAT5 (left graphs) and TERT (right graphs)
612 enrichment on the RUNX2 promoter of control VICs after 14 days of osteogenic stimulation and
613 quantified by ChIP-qPCR. n = 4. D, Representative images of control and CAVD VICs treated
614 with 10 µM of the STAT5 inhibitors StafiA-1or StafiB-1 during 28 days of osteogenic stimulation.
615 Scalebar 400 µm. n = 8, means ± SD. Quantification of calcification is shown on the right graph.
616 Data are shown as means ± SD. *P* values were calculated by the Mann-Whitney *U* test (Figure
617 A and C) and Kruskal-Wallis *H* test (Figure D) and indicated on each graph.

618

619 **Figure 7. TERT and STAT5 are upregulated and colocalize in CAVD tissue.**

620 A, Representative serial sections of Von Kossa (dark precipitation, top panels) and TERT and
621 STAT5 immunofluorescent staining (bottom panels) in control and CAVD valve tissues.
622 Scalebar100 µm. Quantification of STAT5 intensity and STAT5-positive cells (STAT5+) are
623 shown on the right panels. B, Quantification of STAT5-TERT-positive cells. Data are shown as
624 means ± SD, n = 5 control, n = 6 CAVD. *P* values were calculated with the Mann-Whitney *U* test
625 and indicated on each graph.

626

627 **Figure 8. TERT/STAT5 promotes osteogenic reprogramming**

628 Inflammation promotes the upregulation and interaction of TERT and STAT5. Then, the
629 TERT/STAT5 complex translocates into the nucleus where TERT facilitates STAT5 binding to

630 the promoter region of *RUNX2* gene, to engage the osteogenic reprogramming of VICs during
631 the early stages of CAVD pathogenesis.

632

633 **Supplemental Figure 1. Characterization of human CAVD valves and correlation of TERT**
634 **expression with age.** A, Representative section of Von Kossa staining in control and valve
635 CAVD leaflets tissue. Scalebar 1 mm. B, Representative serial sections of RUNX2
636 immunofluorescent staining (top panels) and OPN (bottom panels) in control and CAVD valve
637 tissues. Scalebar 100 µm. Quantification of RUNX2-positive cells and OPN-positive cells on the
638 leaflet specimen is shown on the right graphs. n = 5 control, n = 6 CAVD. C, Correlation
639 between age of the donor and *TERT* expression. n = 8 control, n = 9 CAVD, Pearson correlation
640 test. D, Expression profile in the subject leaflets. n = 7 control, n = 7 CAVD. E, Confocal images
641 of a CAVD leaflet. Scalebar 50 µm. F, Representative images of immunofluorescent staining of
642 PCNA (top panels) and γ-H2AX (bottom panels) in control and CAVD valve tissues. Scalebar
643 100 µm. Quantification of PCNA-positive cells and γ-H2AX-positive cells are shown on the right
644 graphs. n = 4 control, n = 3 CAVD. Data are shown as means ± SD. *P* values were calculated
645 with the Mann-Whitney *U* test (Figures B, G, and F) and two-way ANOVA with the Sidak post
646 hoc test (heatmap on D).

647

648 **Supplemental Figure 2. VIC migration, activation, and osteogenic markers at baseline.**
649 A, Representative images of a scratch assay in control (top panels) and CAVD (bottom panels)
650 VICs. Time points are indicated on top of each panel. Blue lines denote the cell migration front.
651 Scalebar 1 mm. n = 10 control, n = 10 CAVD. B, Representative images of αSMA and CNN (top
652 panels) and SM22 (bottom panels) in control and CAVD VICs. Scalebar 50 µm. Signal

653 quantification of αSMA, CNN, and SM22 are shown on the right panels. n = 4 control, n = 4
654 CAVD. C, Representative images of TNAP and f-Actin signal in control and CAVD VICs.
655 Scalebar 50 µm. Signal quantification of TNAP and f-Actin is shown on the right panels. n = 4
656 control, n = 4 CAVD. Data are shown as means ± SD. *P* values were calculated with the Mann-
657 Whitney *U* test and shown on top of each graph.
658
659 **Supplemental Figure 3. Senescence is not operative during the osteogenic differentiation**
660 **of VICs.**
661 A, Cell counting of control and CAVD VICs after 14 days of NT or OST stimulation. n = 4
662 control, n = 4 CAVD. B, β-galactosidase (*BGLAP*) mRNA transcript quantification in control and
663 CAVD VICs at baseline. n = 5 control, n= 4 CAVD. C, Representative images of senescence-
664 associated β-galactosidase activity staining of VICs after 28 days of NT or OST stimulation.
665 Blue cells were considered positive for senescence. Quantification of senescence is shown on
666 the right graph. n = 4 control; n = 4 CAVD. Data are shown as means ± SD. *P* values were
667 calculated with the Mann-Whitney *U* test (figure A and B) and the Kruskal-Wallis *H* test with
668 Dunn post hoc test and shown on top of each graph.
669
670 **Supplemental Figure 4. TERT is upregulated and required for the osteogenic**
671 **differentiation of human mesenchymal stem cells.**
672 A, Representative images of human MSCs stimulated with OST for 14 days. Calcium deposition
673 was visualized by Alizarin Red staining. Quantification of calcification is shown on the right
674 graph. n = 3. Scalebar 50 µm. B, Western blot staining of samples from MSCs collected during
675 the 14 days of OST treatment. C, TERT and RUNX2 expression profile of differentiating MSCs
676 stimulated for 14 days with OST media. n = 3. D, Representative TERT immunofluorescent
677 staining images of MSCs stimulated with osteogenic media for 14 days. Scalebar 100 µm. E,

678 MSCs transduced with lentivirus containing either shControl-GFP or shTERT-GFP and
679 stimulated with osteogenic media for up to 21 days. Quantification of calcification is shown on
680 the right graph. n = 4; means ± SD. F, Representative western blot staining of MSCs transduced
681 with lentivirus containing either shControl-GFP or shTERT-GFP followed by 7 days of
682 osteogenic stimulation. Data are shown as means ± SD. *P* values were calculated by Kruskal-
683 Wallis *H* test with Dunn pairwise comparison post hoc test (Figure C) and two-way ANOVA with
684 Tukey post hoc test (Figures A and E).
685
686 **Supplemental Figure 5. Senescence is not operative in mice Tert -/- cells.**
687 A, Representative images of a senescence-associated β-galactosidase (SA-β-gal) staining of
688 mVICs isolated from wild-type (*Tert* $^{+/+}$) or F1 Tert knockout (*Tert* $^{-/-}$) mice after 21 days of OST
689 stimulation. Blue cells were considered positive for senescence. Quantification of senescence
690 cells is shown on the right graph. B, Representative images of SA-β-gal staining of mBMMSCs
691 isolated from *Tert* $^{+/+}$ or *Tert* $^{-/-}$ mice after 21 days of osteogenic stimulation. Blue cells were
692 considered positive for senescence. Quantification of senescence is shown on the right graph.
693 Both figures, n = 5 *Tert* $^{+/+}$, n = 3 *Tert* -/-. Scalebar 400 µm. Data are shown as means ± SD. *P*
694 values were calculated with the Mann-Whitney *U* test and shown on each graph.
695
696 **Supplemental Data Fig 6. STAT5 is upregulated and required during osteogenic**
697 **differentiation of VICs.**
698 A, Representative western blot staining of samples from CAVD and control VICs after 14 days of
699 OST stimulation. Quantification of protein levels is shown on the right graphs. n = 4, control n = 4
700 CAVD. B, Representative immunofluorescence image of STAT5 shows subcellular distribution
701 after 14 days of NT and OST stimulation. Scalebar 40 µm. C, Representative images of
702 TERT/STAT5 complex (red foci) in control VICs and detected by proximity ligation assay (PLA).

703 Scalebar 100 µm. Quantification of PLA is shown on the right graph. n = 4. D, Representative
704 images of CASMCs (left panels) treated with 10 µM of the STAT5 inhibitors StafiA-1 or StafiB-1
705 during the 14 days of OST stimulation. Scalebar 400 µm. Quantification of calcification is shown
706 on the right graph. n = 4.E, Representative images of MSCs (left panels) treated with 10 µM of
707 the STAT5 inhibitors StafiA-1 or StafiB-1 during the 21 days of OST stimulation. Scalebar 400
708 µm. Quantification of calcification is shown on the right graph. n = 4. F, Representative
709 immunofluorescence images of VICs after 14 days of LPS treatment or OST stimulation. Scalebar
710 50 µm. G, Representative western blot staining of CAVD VICs after 14 days of OST stimulation.
711 Data are shown as means ± SD. *P* values were calculated with the Mann-Whitney *U* test (Figures
712 A and B) and the Kruskal-Wallis *H* test with Dunn pairwise comparison post-test (Figured D and
713 E) and indicated in each graph.
714

715 **REFERENCES**

716 1. Kraler S, Blaser MC, Aikawa E, Camici GG, Luscher TF. Calcific aortic valve disease:
717 from molecular and cellular mechanisms to medical therapy. *Eur Heart J*. 2022;43:683-
718 697. doi: 10.1093/eurheartj/ehab757
719 2. Buttner P, Feistner L, Lurz P, Thiele H, Hutcheson JD, Schlotter F. Dissecting Calcific
720 Aortic Valve Disease-The Role, Etiology, and Drivers of Valvular Fibrosis. *Front*
721 *Cardiovasc Med*. 2021;8:660797. doi: 10.3389/fcvm.2021.660797
722 3. Coffey S, Roberts-Thomson R, Brown A, Carapetis J, Chen M, Enriquez-Sarano M,
723 Zuhlke L, Prendergast BD. Global epidemiology of valvular heart disease. *Nat Rev*
724 *Cardiol*. 2021;18:853-864. doi: 10.1038/s41569-021-00570-z
725 4. Roth GA, Mensah GA, Johnson CO, Addolorato G, Ammirati E, Baddour LM, Barengo
726 NC, Beaton AZ, Benjamin EJ, Benziger CP, et al. Global Burden of Cardiovascular
727 Diseases and Risk Factors, 1990-2019: Update From the GBD 2019 Study. *J Am Coll*
728 *Cardiol*. 2020;76:2982-3021. doi: 10.1016/j.jacc.2020.11.010
729 5. Yutzey KE, Demer LL, Body SC, Huggins GS, Towler DA, Giachelli CM, Hofmann-
730 Bowman MA, Mortlock DP, Rogers MB, Sadeghi MM, et al. Calcific aortic valve disease:

731 a consensus summary from the Alliance of Investigators on Calcific Aortic Valve
732 Disease. *Arterioscler Thromb Vasc Biol*. 2014;34:2387-2393. doi:
733 10.1161/ATVBAHA.114.302523
734 6. Virani SS, Alonso A, Benjamin EJ, Bittencourt MS, Callaway CW, Carson AP,
735 Chamberlain AM, Chang AR, Cheng S, Delling FN, et al. Heart Disease and Stroke
736 Statistics-2020 Update: A Report From the American Heart Association. *Circulation*.
737 2020;141:e139-e596. doi: 10.1161/CIR.0000000000000757
738 7. Rajamannan NM, Evans FJ, Aikawa E, Grande-Allen KJ, Demer LL, Heistad DD,
739 Simmons CA, Masters KS, Mathieu P, O'Brien KD, et al. Calcific aortic valve disease:
740 not simply a degenerative process: A review and agenda for research from the National
741 Heart and Lung and Blood Institute Aortic Stenosis Working Group. Executive summary:
742 Calcific aortic valve disease-2011 update. *Circulation*. 2011;124:1783-1791. doi:
743 10.1161/CIRCULATIONAHA.110.006767
744 8. Chen JH, Simmons CA. Cell-matrix interactions in the pathobiology of calcific aortic
745 valve disease: critical roles for matricellular, matricrine, and matrix mechanics cues. *Circ*
746 *Res*. 2011;108:1510-1524. doi: 10.1161/CIRCRESAHA.110.234237
747 9. Liu AC, Joag VR, Gotlieb AI. The emerging role of valve interstitial cell phenotypes in
748 regulating heart valve pathobiology. *Am J Pathol*. 2007;171:1407-1418. doi:
749 10.2353/ajpath.2007.070251
750 10. Rajamannan NM, Subramaniam M, Rickard D, Stock SR, Donovan J, Springett M,
751 Orszulak T, Fullerton DA, Tajik AJ, Bonow RO, et al. Human aortic valve calcification is
752 associated with an osteoblast phenotype. *Circulation*. 2003;107:2181-2184. doi:
753 10.1161/01.CIR.0000070591.21548.69
754 11. Rajamannan NM. Calcific aortic valve disease: cellular origins of valve calcification.
755 *Arterioscler Thromb Vasc Biol*. 2011;31:2777-2778. doi: 10.1161/ATVBAHA.111.237610
756 12. Aikawa E, Libby P. A Rock and a Hard Place: Chiseling Away at the Multiple
757 Mechanisms of Aortic Stenosis. *Circulation*. 2017;135:1951-1955. doi:
758 10.1161/CIRCULATIONAHA.117.027776
759 13. Wirrig EE, Yutzey KE. Conserved transcriptional regulatory mechanisms in aortic valve
760 development and disease. *Arterioscler Thromb Vasc Biol*. 2014;34:737-741. doi:
761 10.1161/ATVBAHA.113.302071
762 14. Calado RT, Young NS. Telomere diseases. *N Engl J Med*. 2009;361:2353-2365. doi:
763 10.1056/NEJMra0903373

764 15. Stewart SA, Hahn WC, O'Connor BF, Banner EN, Lundberg AS, Modha P, Mizuno H,
765 Brooks MW, Fleming M, Zimonjic DB, et al. Telomerase contributes to tumorigenesis by
766 a telomere length-independent mechanism. *Proc Natl Acad Sci U S A*. 2002;99:12606-
767 12611. doi: 10.1073/pnas.182407599
768 16. Choi J, Southworth LK, Sarin KY, Venteicher AS, Ma W, Chang W, Cheung P, Jun S,
769 Artandi MK, Shah N, et al. TERT promotes epithelial proliferation through transcriptional
770 control of a Myc- and Wnt-related developmental program. *PLoS Genet*. 2008;4:e10.
771 doi: 10.1371/journal.pgen.0040010
772 17. Masutomi K, Possemato R, Wong JM, Currier JL, Tothova Z, Manola JB, Ganesan S,
773 Lansdorp PM, Collins K, Hahn WC. The telomerase reverse transcriptase regulates
774 chromatin state and DNA damage responses. *Proc Natl Acad Sci U S A*.
775 2005;102:8222-8227. doi: 10.1073/pnas.0503095102
776 18. Park JI, Venteicher AS, Hong JY, Choi J, Jun S, Shkreli M, Chang W, Meng Z, Cheung
777 P, Ji H, et al. Telomerase modulates Wnt signalling by association with target gene
778 chromatin. *Nature*. 2009;460:66-72. doi: 10.1038/nature08137
779 19. Aono J, Ruiz-Rodriguez E, Qing H, Findeisen HM, Jones KL, Heywood EB, Bruemmer
780 D. Telomerase Inhibition by Everolimus Suppresses Smooth Muscle Cell Proliferation
781 and Neointima Formation Through Epigenetic Gene Silencing. *JACC Basic Transl Sci*.
782 2016;1:49-60. doi: 10.1016/j.jacbts.2016.01.002
783 20. Endorf EB, Qing H, Aono J, Terami N, Doyon G, Hyzny E, Jones KL, Findeisen HM,
784 Bruemmer D. Telomerase Reverse Transcriptase Deficiency Prevents Neointima
785 Formation Through Chromatin Silencing of E2F1 Target Genes. *Arterioscler Thromb*
786 *Vasc Biol*. 2017;37:301-311. doi: 10.1161/ATVBAHA.116.308717
787 21. Shi S, Gronthos S, Chen S, Reddi A, Counter CM, Robey PG, Wang CY. Bone
788 formation by human postnatal bone marrow stromal stem cells is enhanced by
789 telomerase expression. *Nat Biotechnol*. 2002;20:587-591. doi: 10.1038/nbt0602-587
790 22. Simonsen JL, Rosada C, Serakinci N, Justesen J, Stenderup K, Rattan SI, Jensen TG,
791 Kassem M. Telomerase expression extends the proliferative life-span and maintains the
792 osteogenic potential of human bone marrow stromal cells. *Nat Biotechnol*. 2002;20:592-
793 596. doi: 10.1038/nbt0602-592
794 23. Cuevas RA, Chu CC, Moorhead WJ, 3rd, Wong R, Sultan I, St Hilaire C. Isolation of
795 Human Primary Valve Cells for In vitro Disease Modeling. *J Vis Exp*. 2021:e62439. doi:
796 10.3791/62439

797 24. Ducy P, Zhang R, Geoffroy V, Ridall AL, Karsenty G. Osf2/Cbfa1: a transcriptional
798 activator of osteoblast differentiation. *Cell*. 1997;89:747-754. doi: 10.1016/s0092-
799 8674(00)80257-3
800 25. Sun Y, Byon CH, Yuan K, Chen J, Mao X, Heath JM, Javed A, Zhang K, Anderson PG,
801 Chen Y. Smooth muscle cell-specific runx2 deficiency inhibits vascular calcification. *Circ*
802 *Res*. 2012;111:543-552. doi: 10.1161/CIRCRESAHA.112.267237
803 26. Parra-Izquierdo I, Castanos-Mollor I, Lopez J, Gomez C, San Roman JA, Sanchez
804 Crespo M, Garcia-Rodriguez C. Calcification Induced by Type I Interferon in Human
805 Aortic Valve Interstitial Cells Is Larger in Males and Blunted by a Janus Kinase Inhibitor.
806 *Arterioscler Thromb Vasc Biol*. 2018;38:2148-2159. doi: 10.1161/ATVBAHA.118.311504
807 27. Parra-Izquierdo I, Castanos-Mollor I, Lopez J, Gomez C, San Roman JA, Sanchez
808 Crespo M, Garcia-Rodriguez C. Lipopolysaccharide and interferon-gamma team up to
809 activate HIF-1alpha via STAT1 in normoxia and exhibit sex differences in human aortic
810 valve interstitial cells. *Biochim Biophys Acta Mol Basis Dis*. 2019;1865:2168-2179. doi:
811 10.1016/j.bbadis.2019.04.014
812 28. Jin H, St Hilaire C, Huang Y, Yang D, Dmitrieva NI, Negro A, Schwartzbeck R, Liu Y, Yu
813 Z, Walts A, et al. Increased activity of TNAP compensates for reduced adenosine
814 production and promotes ectopic calcification in the genetic disease ACDC. *Sci Signal*.
815 2016;9:ra121. doi: 10.1126/scisignal.aaf9109
816 29. Moorhead WJ, 3rd, Chu CC, Cuevas RA, Callahan Jt, Wong R, Regan C, Boufford CK,
817 Sur S, Liu M, Gomez D, et al. Dysregulation of FOXO1 (Forkhead Box O1 Protein)
818 Drives Calcification in Arterial Calcification due to Deficiency of CD73 and Is Present in
819 Peripheral Artery Disease. *Arterioscler Thromb Vasc Biol*. 2020;40:1680-1694. doi:
820 10.1161/ATVBAHA.119.313765
821 30. Jung JJ, Razavian M, Kim HY, Ye Y, Golestani R, Toczek J, Zhang J, Sadeghi MM.
822 Matrix metalloproteinase inhibitor, doxycycline and progression of calcific aortic valve
823 disease in hyperlipidemic mice. *Sci Rep*. 2016;6:32659. doi: 10.1038/srep32659
824 31. Millan A, Lanzer P, Sorribas V. The Thermodynamics of Medial Vascular Calcification.
825 *Front Cell Dev Biol*. 2021;9:633465. doi: 10.3389/fcell.2021.633465
826 32. Kim NW, Piatyszek MA, Prowse KR, Harley CB, West MD, Ho PL, Coviello GM, Wright
827 WE, Weinrich SL, Shay JW. Specific association of human telomerase activity with
828 immortal cells and cancer. *Science*. 1994;266:2011-2015. doi: 10.1126/science.7605428

829 33. Hao LY, Armanios M, Strong MA, Karim B, Feldser DM, Huso D, Greider CW. Short
830 telomeres, even in the presence of telomerase, limit tissue renewal capacity. *Cell*.
831 2005;123:1121-1131. doi: 10.1016/j.cell.2005.11.020
832 34. Pascolo E, Wenz C, Lingner J, Hauel N, Priepke H, Kauffmann I, Garin-Chesa P, Rettig
833 WJ, Damm K, Schnapp A. Mechanism of human telomerase inhibition by BIBR1532, a
834 synthetic, non-nucleosidic drug candidate. *J Biol Chem*. 2002;277:15566-15572. doi:
835 10.1074/jbc.M201266200
836 35. Ogawa D, Nomiyama T, Nakamachi T, Heywood EB, Stone JF, Berger JP, Law RE,
837 Bruemmer D. Activation of peroxisome proliferator-activated receptor gamma
838 suppresses telomerase activity in vascular smooth muscle cells. *Circ Res*. 2006;98:e50-
839 59. doi: 10.1161/01.RES.0000218271.93076.c3
840 36. Chiang YJ, Hemann MT, Hathcock KS, Tessarollo L, Feigenbaum L, Hahn WC, Hodes
841 RJ. Expression of telomerase RNA template, but not telomerase reverse transcriptase,
842 is limiting for telomere length maintenance in vivo. *Mol Cell Biol*. 2004;24:7024-7031.
843 doi: 10.1128/MCB.24.16.7024-7031.2004
844 37. Ghosh A, Saginc G, Leow SC, Khattar E, Shin EM, Yan TD, Wong M, Zhang Z, Li G,
845 Sung WK, et al. Telomerase directly regulates NF-kappaB-dependent transcription. *Nat*
846 *Cell Biol*. 2012;14:1270-1281. doi: 10.1038/ncb2621
847 38. Liu N, Ding D, Hao W, Yang F, Wu X, Wang M, Xu X, Ju Z, Liu JP, Song Z, et al. hTERT
848 promotes tumor angiogenesis by activating VEGF via interactions with the Sp1
849 transcription factor. *Nucleic Acids Res*. 2016;44:8693-8703. doi: 10.1093/nar/gkw549
850 39. Lee C, Huang CH. LASAGNA: a novel algorithm for transcription factor binding site
851 alignment. *BMC Bioinformatics*. 2013;14:108. doi: 10.1186/1471-2105-14-108
852 40. Wingender E, Dietze P, Karas H, Knuppel R. TRANSFAC: a database on transcription
853 factors and their DNA binding sites. *Nucleic Acids Res*. 1996;24:238-241. doi:
854 10.1093/nar/24.1.238
855 41. Okutani Y, Kitanaka A, Tanaka T, Kamano H, Ohnishi H, Kubota Y, Ishida T, Takahara
856 J. Src directly tyrosine-phosphorylates STAT5 on its activation site and is involved in
857 erythropoietin-induced signaling pathway. *Oncogene*. 2001;20:6643-6650. doi:
858 10.1038/sj.onc.1204807
859 42. Natarajan K, Muller-Klieser D, Rubner S, Berg T. Stafia-1: a STAT5a-Selective Inhibitor
860 Developed via Docking-Based Screening of in Silico O-Phosphorylated Fragments.
861 *Chemistry*. 2020;26:148-154. doi: 10.1002/chem.201904147

862 43. Elumalai N, Berg A, Natarajan K, Scharow A, Berg T. Nanomolar inhibitors of the
863 transcription factor STAT5b with high selectivity over STAT5a. *Angew Chem Int Ed Engl*.
864 2015;54:4758-4763. doi: 10.1002/anie.201410672
865 44. Leopold JA. Cellular mechanisms of aortic valve calcification. *Circ Cardiovasc Interv*.
866 2012;5:605-614. doi: 10.1161/CIRCINTERVENTIONS.112.971028
867 45. Babu AN, Meng X, Zou N, Yang X, Wang M, Song Y, Cleveland JC, Weyant M,
868 Banerjee A, Fullerton DA. Lipopolysaccharide stimulation of human aortic valve
869 interstitial cells activates inflammation and osteogenesis. *Ann Thorac Surg*. 2008;86:71-
870 76. doi: 10.1016/j.athoracsur.2008.03.008
871 46. Gizard F, Nomiyama T, Zhao Y, Findeisen HM, Heywood EB, Jones KL, Staels B,
872 Bruemmer D. The PPARalpha/p16INK4a pathway inhibits vascular smooth muscle cell
873 proliferation by repressing cell cycle-dependent telomerase activation. *Circ Res*.
874 2008;103:1155-1163. doi: 10.1161/CIRCRESAHA.108.186205
875 47. Maida Y, Yasukawa M, Okamoto N, Ohka S, Kinoshita K, Totoki Y, Ito TK, Minamino T,
876 Nakamura H, Yamaguchi S, et al. Involvement of telomerase reverse transcriptase in
877 heterochromatin maintenance. *Mol Cell Biol*. 2014;34:1576-1593. doi:
878 10.1128/MCB.00093-14
879 48. Okamoto N, Yasukawa M, Nguyen C, Kasim V, Maida Y, Possemato R, Shibata T, Ligon
880 KL, Fukami K, Hahn WC, et al. Maintenance of tumor initiating cells of defined genetic
881 composition by nucleostemin. *Proc Natl Acad Sci U S A*. 2011;108:20388-20393. doi:
882 10.1073/pnas.1015171108
883 49. Slagboom PE, Droog S, Boomsma DI. Genetic determination of telomere size in
884 humans: a twin study of three age groups. *Am J Hum Genet*. 1994;55:876-882.
885 50. Brouilette S, Singh RK, Thompson JR, Goodall AH, Samani NJ. White cell telomere
886 length and risk of premature myocardial infarction. *Arterioscler Thromb Vasc Biol*.
887 2003;23:842-846. doi: 10.1161/01.ATV.0000067426.96344.32
888 51. Samani NJ, Boultby R, Butler R, Thompson JR, Goodall AH. Telomere shortening in
889 atherosclerosis. *Lancet*. 2001;358:472-473. doi: 10.1016/S0140-6736(01)05633-1
890 52. Kurz DJ, Kloeckener-Gruissem B, Akhmedov A, Eberli FR, Buhler I, Berger W, Bertel O,
891 Luscher TF. Degenerative aortic valve stenosis, but not coronary disease, is associated
892 with shorter telomere length in the elderly. *Arterioscler Thromb Vasc Biol*. 2006;26:e114-
893 117. doi: 10.1161/01.ATV.0000222961.24912.69

894 53. Huzen J, Peeters W, de Boer RA, Moll FL, Wong LS, Codd V, de Kleijn DP, de Smet BJ,
895 van Veldhuisen DJ, Samani NJ, et al. Circulating leukocyte and carotid atherosclerotic
896 plaque telomere length: interrelation, association with plaque characteristics, and
897 restenosis after endarterectomy. *Arterioscler Thromb Vasc Biol*. 2011;31:1219-1225. doi:
898 10.1161/ATVBAHA.110.217158
899 54. Hoerstrup SP, Kadner A, Melnitchouk S, Trojan A, Eid K, Tracy J, Sodian R, Visjager JF,
900 Kolb SA, Grunenfelder J, et al. Tissue engineering of functional trileaflet heart valves
901 from human marrow stromal cells. *Circulation*. 2002;106:I143-150.
902 55. Hortells L, Sur S, St Hilaire C. Cell Phenotype Transitions in Cardiovascular
903 Calcification. *Front Cardiovasc Med*. 2018;5:27. doi: 10.3389/fcvm.2018.00027
904 56. Bogdanova M, Zabirnyk A, Malashicheva A, Enayati KZ, Karlsen TA, Kaljusto ML,
905 Kvitting JP, Dissen E, Sullivan GJ, Kostareva A, et al. Interstitial cells in calcified aortic
906 valves have reduced differentiation potential and stem cell-like properties. *Sci Rep*.
907 2019;9:12934. doi: 10.1038/s41598-019-49016-0
908 57. Lin ME, Chen T, Leaf EM, Speer MY, Giachelli CM. Runx2 Expression in Smooth
909 Muscle Cells Is Required for Arterial Medial Calcification in Mice. *Am J Pathol*.
910 2015;185:1958-1969. doi: 10.1016/j.ajpath.2015.03.020
911 58. Xu K, Xie S, Huang Y, Zhou T, Liu M, Zhu P, Wang C, Shi J, Li F, Sellke FW, et al. Cell-
912 Type Transcriptome Atlas of Human Aortic Valves Reveal Cell Heterogeneity and
913 Endothelial to Mesenchymal Transition Involved in Calcific Aortic Valve Disease.
914 *Arterioscler Thromb Vasc Biol*. 2020;40:2910-2921. doi: 10.1161/ATVBAHA.120.314789
915 59. Joung YH, Lim EJ, Darvin P, Chung SC, Jang JW, Do Park K, Lee HK, Kim HS, Park T,
916 Yang YM. MSM enhances GH signaling via the Jak2/STAT5b pathway in osteoblast-like
917 cells and osteoblast differentiation through the activation of STAT5b in MSCs. *PLoS*
918 *One*. 2012;7:e47477. doi: 10.1371/journal.pone.0047477
919 60. Lee KM, Park KH, Hwang JS, Lee M, Yoon DS, Ryu HA, Jung HS, Park KW, Kim J,
920 Park SW, et al. Inhibition of STAT5A promotes osteogenesis by DLX5 regulation. *Cell*
921 *Death Dis*. 2018;9:1136. doi: 10.1038/s41419-018-1184-7
922 61. Paulson M, Pisharody S, Pan L, Guadagno S, Mui AL, Levy DE. Stat protein
923 transactivation domains recruit p300/CBP through widely divergent sequences. *J Biol*
924 *Chem*. 1999;274:25343-25349. doi: 10.1074/jbc.274.36.25343

925 62. Martino A, Holmes JHt, Lord JD, Moon JJ, Nelson BH. Stat5 and Sp1 regulate
926 transcription of the cyclin D2 gene in response to IL-2. *J Immunol*. 2001;166:1723-1729.
927 doi: 10.4049/jimmunol.166.3.1723
928 63. Bergad PL, Towle HC, Berry SA. Yin-yang 1 and glucocorticoid receptor participate in
929 the Stat5-mediated growth hormone response of the serine protease inhibitor 2.1 gene.
930 *J Biol Chem*. 2000;275:8114-8120. doi: 10.1074/jbc.275.11.8114
931 64. Yamada O, Ozaki K, Furukawa T, Machida M, Wang YH, Motoji T, Mitsuishi T, Akiyama
932 M, Yamada H, Kawauchi K, et al. Activation of STAT5 confers imatinib resistance on
933 leukemic cells through the transcription of TERT and MDR1. *Cell Signal*. 2011;23:1119-
934 1127. doi: 10.1016/j.cellsig.2011.02.005
935 65. Yamada O, Ozaki K, Akiyama M, Kawauchi K. JAK-STAT and JAK-PI3K-mTORC1
936 pathways regulate telomerase transcriptionally and posttranslationally in ATL cells. *Mol*
937 *Cancer Ther*. 2012;11:1112-1121. doi: 10.1158/1535-7163.MCT-11-0850
938 66. Tormo AJ, Letellier MC, Sharma M, Elson G, Crabe S, Gauchat JF. IL-6 activates
939 STAT5 in T cells. *Cytokine*. 2012;60:575-582. doi: 10.1016/j.cyto.2012.07.002
940 67. Tanabe Y, Nishibori T, Su L, Arduini RM, Baker DP, David M. Cutting edge: role of
941 STAT1, STAT3, and STAT5 in IFN-alpha beta responses in T lymphocytes. *J Immunol*.
942 2005;174:609-613. doi: 10.4049/jimmunol.174.2.609
943 68. Honda S, Miyamoto T, Watanabe T, Narumi T, Kadowaki S, Honda Y, Otaki Y,
944 Hasegawa H, Netsu S, Funayama A, et al. A novel mouse model of aortic valve stenosis
945 induced by direct wire injury. *Arterioscler Thromb Vasc Biol*. 2014;34:270-278. doi:
946 10.1161/ATVBAHA.113.302610
947 69. Sider KL, Blaser MC, Simmons CA. Animal models of calcific aortic valve disease. *Int J*
948 *Inflam*. 2011;2011:364310. doi: 10.4061/2011/364310
949 70. Balani K, Brito FC, Kos L, Agarwal A. Melanocyte pigmentation stiffens murine cardiac
950 tricuspid valve leaflet. *J R Soc Interface*. 2009;6:1097-1102. doi: 10.1098/rsif.2009.0174
951 71. Carneiro F, Kruithof BP, Balani K, Agarwal A, Gaussin V, Kos L. Relationships between
952 melanocytes, mechanical properties and extracellular matrix composition in mouse heart
953 valves. *J Long Term Eff Med Implants*. 2015;25:17-26. doi:
954 10.1615/jlongtermeffmedimplants.2015011748
955 72. Mjaatvedt CH, Kern CB, Norris RA, Fairey S, Cave CL. Normal distribution of
956 melanocytes in the mouse heart. *Anat Rec A Discov Mol Cell Evol Biol*. 2005;285:748-
957 757. doi: 10.1002/ar.a.20210

958 73. Dharmarajan S, Speer MY, Pierce K, Lally J, Leaf EM, Lin ME, Scatena M, Giachelli CM.
959 Role of Runx2 in Calcific Aortic Valve Disease in Mouse Models. *Front Cardiovasc Med*.
960 2021;8:687210. doi: 10.3389/fcvm.2021.687210
961

SUPPLEMENTAL MATERIAL

Non-canonical Telomerase Reverse Transcriptase Controls Osteogenic Differentiation of Aortic Valve Cells Through STAT5

Rolando A. Cuevas[1], Luis Hortells[1,2], Claire C. Chu[1], Ryan Wong[1], Alex Crane[1], Camille Boufford[1], Cailyn Regan[1], William J. Moorhead III[1], Michael J. Bashline[1], Aneesha Parwal[1], Angelina M. Parise[1], Aditi Gurkar[3], Dennis Bruemmer[4], John Sembrat[5], Ibrahim Sultan[6], Thomas G. Gleason[7], Marie Billaud[8], and Cynthia St. Hilaire[1,9*]

[1] Division of Cardiology, Department of Medicine, Pittsburgh Heart, Lung, Blood and Vascular Medicine Institute, University of Pittsburgh, Pittsburgh, Pennsylvania, USA.

[2] current address - Institute for Experimental Cardiovascular Medicine, University Heart Centre Freiburg–Bad Krozingen, Medical Center and Faculty of Medicine, University of Freiburg, Freiburg, Germany.

[3] Aging Institute, Division of Geriatrics, Department of Medicine, University of Pittsburgh, Pittsburgh, Pennsylvania, USA.

[4] Department of Cardiovascular Medicine, Cleveland Clinic, Cleveland, OH, USA.

[5] Division of Pulmonary, Allergy, and Critical Care Medicine, University of Pittsburgh School of Medicine, Pittsburgh, PA, USA.

[6] Division of Cardiac Surgery, Department of Cardiothoracic Surgery, Heart and Vascular Institute, University of Pittsburgh Medical Center, Pittsburgh, Pennsylvania, USA.

[7] Division of Cardiac Surgery, Univ. of Maryland School of Medicine, Baltimore, MD, USA.

[8] Department of Surgery, Division of Cardiac Surgery, Brigham and Women's Hospital & Harvard Medical School, Boston, Maryland, USA.

[9] Department of Bioengineering, University of Pittsburgh, Pittsburgh, Pennsylvania, USA.

Running Title: TERT/STAT5 is required for cardiovascular calcification

*Corresponding Author Contact Info:
Cynthia St. Hilaire, PhD, FAHA
University of Pittsburgh
BSTWR 1744.1
200 Lothrop Street, Pittsburgh, PA 15261
+1 412-648-9441 sthilair@pitt.edu

*Corresponding Author Contact Info:
Cynthia St. Hilaire, PhD, FAHA
University of Pittsburgh
BSTWR 1744.1
200 Lothrop Street, Pittsburgh, PA 15261
+1 412-648-9441 sthilair@pitt.edu

METHODS

Availability of Materials

We abide by the NIH Grants Policy on Sharing of Unique Research Resources, including the NIH Policy on Sharing of Model Organisms for Biomedical Research (2004), NIH Grants Policy Statement (2003), and Sharing of Biomedical Research Resources: Principles and Guidelines for Recipients of NIH Grants and Contracts (1999), and the Bayh-Dole Act and the Technology Transfer Commercialization Act of 2000. De-identified human cell lines and tissues generated in our laboratory will be made available for non-commercial research per established University of Pittsburgh Office of Research IRB and MTA protocols.

Ethics

Human aortic valves were collected from subjects enrolled in studies approved by the institutional review board (IRB) of the University of Pittsburgh per the Declaration of Helsinki. No bicuspid valves were used in this study. Mice used for the generation of cell lines were given veterinary care by the University of Pittsburgh Division of Laboratory Animal Resources which adheres to the NIH policy on the Animal Welfare Act and all other applicable laws. Facilities are under the full-time supervision of veterinarians and are AAALAC-accredited. Our protocols follow the AVMA Guidelines on Euthanasia. All animal use was approved by the Institutional Animal Care and Use Committee at the University of Pittsburgh.

Human Tissue Collection and Isolation

Surgical specimens from humans were collected from subjects who consented and enrolled in studies approved by the institutional review board (IRB) of the University of Pittsburgh per the

68 Declaration of Helsinki. Personnel involved with specimen handling underwent extensive
69 institutional training. Cadaveric tissues obtained via the Center for Organ Recovery and
70 Education (CORE) were approved by the University of Pittsburgh Committee for Oversight of
71 Research and Clinical Training Involving Decedents (CORID). A detailed protocol describing
72 tissue collection handling was published previously.[1] Briefly, valves were collected from valve
73 replacement surgeries or recovered from cadaveric organs and stored in cold Belzer UW Cold
74 Storage Transplant Solution (Bridge to Life) at 4°C for transporting. Aortic roots were excised
75 and washed with a sterile rinsing solution (sterile PBS supplemented with 2.5 µg/mL of
76 fungicide, 0.05 mg/mL of gentamicin, and 5 µg/mL of bactericide). Leaflets were unbiasedly
77 selected for VIC isolation, Von Kossa staining for calcification, and snap freezing for RNA
78 collection. Tissues were processed as close as possible to the time of extraction to guarantee
79 the best yield of cell recovery.
80
81 **Human Cell Isolation**
82 We established patient-specific lines by using the same valves for histopathology, RNA, and cell
83 isolation. Human primary aortic valve interstitial cell (VIC) lines were generated from male and
84 female subjects as previously described.[2] Briefly, leaflets were washed with PBS containing 10
85 mg/ml gentamicin (GIBCO) and 250 µg/ml fungizone (GIBCO) and dissociated with 0.1%
86 collagenase II at 37 C and 5% of CO2 for 18 hours. Then, the tissue was further dissociated by
87 gently mixing it by pipetting with a serological pipette to ensure the release of AVICs and then
88 passed through a 0.70 µm filter to remove debris. Cells were pelleted and then resuspended in
89 Dulbecco's Modified Eagle's Medium (DMEM) supplemented with 10% fetal bovine serum (FBS)
90 and 1X penicillin-streptomycin (P/S). Human coronary artery smooth muscle cells (CASMC)
91 were obtained from the patient coronary as previously described.[3] Briefly, vessels were washed

92 with PBS containing 10 mg/ml gentamicin (GIBCO) and 250 µg/ml fungizone (GIBCO). Vessels
93 were cut open to expose the lumen and intima and adventitia were gently scrapped. Vessels
94 were then sectioned and dissociated with 0.1% collagenase II for 3 hrs. Cells were pelleted and
95 then seeded and expanded.
96
97 **Cell Culture**
98 VIC lines were expanded in Dulbecco's Modified Eagle's Medium supplemented with 10% fetal
99 bovine serum and 1X penicillin-streptomycin. Cells were used between passages 4 and 15.
100 Growth media was changed every three days, and cells were split 1:2 when confluent. Human
101 coronary artery smooth muscle cell (CASMC) lines were expanded in smooth muscle media
102 SMGM (CC-3181) supplemented with BULLETKIT (CC-4149). Human mesenchymal stem cells
103 (MSCs, PT-2501, Lonza) were expanded on Minimum Essential Medium alpha without
104 nucleosides and supplemented with 10% fetal bovine serum and 1X penicillin-streptomycin and
105 used between passages 4 and 10. Cells are routinely tested for mycoplasma contamination.
106
107 **Osteogenic Assay**
108 For osteogenic experiments, 250,000 cells per 9.5 cm^2 were seeded and treated with
109 osteogenic media (Gibco Minimum Essential Medium alpha with nucleosides, 10% FBS, 1X
110 P/S, 10 mM glycerol phosphate, 50 µM ascorbic acid 2-phosphate, and 100 nM
111 dexamethasone).[4] No treatment media consisted of Gibco Minimum Essential Medium alpha
112 with nucleosides, 10% FBS, 1X P/S. Media was replaced every four days and prepared fresh
113 every time. BiBR1532 (2981, Tocris) was added to the media at 1, 10, or 100 nM every two
114 days during the OST treatment.[5] Inhibitors StafiA-1 and StafiB-1 (Sigma-Aldrich) were used at
115 10 µM and added every two days for the duration of the OST treatment. For inflammatory

116 assays, we used 2.5 µg/mL of LPS from Escherichia coli O111:B4 (Sigma-Aldrich) every two
117 days for the duration of the OST treatment.
118
119 **SDS-Page and Immunoblotting**
120 Cells were lysed in lysis buffer (1% CHAPS hydrate, 150 mM sodium chloride, 25 mM HEPES
121 buffer), supplemented with 1x protease and phosphatase inhibitor cocktail (Sigma-Aldrich).
122 Cells were scraped and transferred into microcentrifuge tubes, vortexed for 10 minutes,
123 freeze/thawed for 5 cycles, then centrifuged at 12,000 x g for 10 minutes at 4°C, and
124 supernatants were collected. Proteins were separated with TGX 4-20% stain-free
125 polyacrylamide gel (Bio-Rad) in 1x Tris/Glycine/SDS buffer (Bio-Rad) and transferred to 0.2 um
126 nitrocellulose (1620112, Bio-Rad) membrane in 1x Trans-Blot Turbo Transfer Buffer (Bio-Rad)
127 using the Trans-Blot Turbo Transfer System (Bio-Rad) according to the manufacturer
128 recommendations. The membranes were blocked in Odyssey blocking buffer (PBS) (Li-COR)
129 and immunoblotted overnight with primary antibodies against TERT (600-401-252, Rockland),
130 STAT5 (9420S, Cell Signaling), RUNX2 (ab192256, Abcam), MYH11(MAB20221, Abnova),
131 OPN (AF808, R&D systems), αSMA (ab5494, Abcam), TNAP (MAB2909, R&D systems), a-
132 tubulin (926-42213, LI-COR), followed by secondary anti-rabbit or anti-mouse IgG antibody
133 (926-68070, 926-68021, 926-32211, LI-COR). Primary and secondary antibodies were diluted in
134 Odyssey blocking buffer with 0.1% Tween 20. Membranes were washed in PBS with 0.1%
135 Tween 20. Immunofluorescence signals were detected with the Odyssey CLx system (LI-COR),
136 and images were analyzed with Image Studio (Version 5.2, LI-COR).
137
138 **Immunofluorescent Staining on Fixed Cells**
139 Cells were washed with PBS and then fixed with 4% paraformaldehyde (Electron Microscopy
140 Sciences) for 15 minutes at room temperature, followed by 10 minutes of permeabilization with

141 TRITON X-100 0.5% (Fisher Scientific). Cells were incubated at room temperature for 1 hour in
142 blocking buffer (PBS, 0.5% Triton-X 100, 5% FBS). Primary antibodies were diluted in the
143 blocking solution and then incubated overnight at 4°C. Next, cells were washed three times for
144 five minutes each with PBS containing 0.1% TWEEN. Fluorescent secondary antibodies were
145 diluted in blocking solution and incubated for one hour protected from the light, then washed
146 three times for five minutes each with PBS, 0.1% TWEEN 20 with a final wash in PBS.
147 Specimens were finally mounted with Fluoroshield Mounting Medium with DAPI (Abcam) and
148 imaged within 24 hours. F-Actin was stained with AlexaFluor488 Phalloidin (Molecular Probes)
149 for 30 minutes, then washed with PBS before mounting. Calcium accumulation was determined
150 with OsteoImage (Lonza) following the manufacturer's recommendations.
151
152 **Immunofluorescent Staining on Paraffin Sections**
153 Human specimens embedded in paraffin were warmed to 65°C and deparaffinized using xylene
154 and graded alcohol baths, rehydrated in distilled H_2O, and boiled for 20 minutes in antigen
155 unmasking solution (Vector Labs). Cooled samples were then washed with PBS for five
156 minutes. Specimens were then blocked with PBS containing 3% fish skin gelatin and 10% horse
157 serum for one hour. Primary antibodies were diluted in the blocking solution and then incubated
158 overnight at 4°C. Next, specimens were washed three times for five minutes each with PBS
159 containing 3% fish skin gelatin and 0.1% TWEEN 20. Fluorescent secondary antibodies were
160 diluted in a blocking solution and incubated for one hour protected from the light, then washed
161 three times for five minutes each. Specimens were finally mounted with Fluoroshield Mounting
162 Medium with DAPI (Abcam) and imaged within 24 hours.
163
164 **Alizarin Red Staining and Quantification**

165 Cells were washed with PBS and then fixed with 4% paraformaldehyde (Electron Microscopy
166 Sciences) for 15 minutes at room temperature, followed by two washes with deionized water.
167 Fixed cells were then covered with 40 mM Alizarin Red S (Sigma-Aldrich) at pH 4.1 – 4.3 and
168 gently rocked for 20 minutes at room temperature. Cells were then washed twice with deionized
169 water to remove any unincorporated dye. After imaging, Alizarin Red S was extracted with 10%
170 (v/v) acetic acid (Fisher Scientific) for 30 minutes, scraped into a microcentrifuge tube, vortexed,
171 and then incubated at 85°C for 10 minutes. After chilling on ice for 5 minutes, the mixture was
172 centrifuged at 20,000 x g for 15 minutes at 4°C. 500 µl of supernatant was transferred to a new
173 tube, and 10% (v/v) ammonium hydroxide (Fisher Scientific) was then added to the supernatant.
174 Absorbance was at 405 nm using a 96-well plate spectrophotometer.
175
176 **Von Kossa Staining**
177 Human specimens embedded in paraffin were warmed to 65°C for one hour and then
178 deparaffinized through xylene and graded alcohol incubations. Specimens were then
179 rehydrated in distilled water. Specimens were stained using the Von Kossa Method of Calcium
180 Kit (Polysciences, 24633-1) following the manufacturer's instructions.
181
182 **Lentiviral Production and Cell Infection**
183 Lentiviruses were produced by transfecting Dharmacon SMARTvector Lentiviral plasmids
184 encoding shTERT TurboGFP (V3SH11240-225610522) or SMARTvector Non-targeting Control
185 (VSC11707) into HEK293T cells following manufacturer recommendations. The viral-containing
186 supernatant was collected at 48h after transfection, filtered through a 0.45-µm filter, and stored
187 at -80C. Human VICs, CASMCs, and MSCs lines were transduced with MOI of 5 in the
188 presence of 0.8 $\mu g\, ml^{-1}$ polybrene (Millipore) to enhance transduction efficiency.
189

190 **Transcriptional Analysis**

191 Tissue RNA was isolated using Trizol (Life Technologies). Cell RNA was isolated using Quick-
192 RNA MiniPrep (Zymo Research). RNA was treated with DNAse I (Zymo Research) in
193 accordance with the manufacturer's instructions. Reverse transcription was performed using
194 MultiScribe Reverse Transcriptase system (Applied Biosystems). Sixteen ng of cDNA was used
195 per reaction. qPCR was performed on a CFX Connect Real-Time System (Bio-Rad) using
196 PowerUP SYBR Green Master Mix (Applied Biosystems) as follows: one cycle at 95 °C
197 (10 minutes) and 40 cycles of 95 °C (20 seconds) and 58 °C (20 seconds) and 72°C (1 minutes).
198 *GAPDH* or *18s* expression were used to normalize expression. Relative expression was
199 calculated using the average threshold cycle number and the $2^{(Ct(housekeeping\ gene)-Ct(target\ gene))}$
200 formula. Primers are listed in Supplementary Table 1.

201

202 **Telomere Length Analysis**

203 Tissue and AVICs genomic DNA was isolated from passage 1 using DirectAmp Tissue Genomic
204 DNA Amplification Kit (Denville Scientific). Telomere length was analyzed using real-time PCR
205 as previously described.[6] Briefly, genomic DNA was isolated following standard protocol, and 10
206 ng of gDNA per reaction was utilized. Samples were run in triplicate with 35 ng of DNA per
207 reaction, and telomere repeats were amplified using PowerUP SYBR Green Master Mix
208 (Thermofisher Scientific) on a CFX Connect Real-Time PCR System (Bio-Rad). Repeated
209 amplification data were normalized to *RPLP0*/*36b4* as a single copy-gene. Primers are listed in
210 Supplementary Table 1.

211

212 **Proliferation Assays**

213 Cell proliferation was evaluated using Trypan Blue incorporation in an automatized cell counter
214 Countess II FL (Invitrogen). Briefly, cells were grown on alpha-MEM supplemented with 10% of

215 FBS and penicillin and streptomycin cocktail (GIBCO) for the duration of the assay. Growth was
216 quantified twice a week. Cell number during OST treatment was determined at the beginning
217 and end of the assay.
218
219 **Senescence-Associated β-Galactosidase Assays**
220 Cellular senescence was evaluated by senescence-associated β-Galactosidase (SA-β-Gal)
221 activity assay. Briefly, cells were washed with PBS and then fixed with 4% paraformaldehyde
222 (Electron Microscopy Sciences) for 5 minutes at room temperature and then washed twice with
223 PBS. Next, cells were incubated in X-Gal Solution Mix containing 1 mg/mL of 5-Bromo-4-
224 Chloro-3-Indolyl-Alpha-D-Galactopyranoside (American Bioanalytical), 40 mM Sodium
225 Phosphate monobasic solution (Sigma-Aldrich), 40 mM Sodium Phosphate Dibasic solution
226 (Sigma-Aldrich), 40 mM Citric Acid (Sigma-Aldrich), 5 mM Potassium Ferrocyanaide (Sigma-
227 Aldrich), 5 mM Potassium Ferricyanaide (Sigma-Aldrich), 150 mM $NaCl_2$, and 2 mM $MgCl_2$, pH
228 6.0, for 16 hours at 37°C without CO_2 to develop blue color. Then, cells were washed twice with
229 PBS, and SA-*β*-gal positive cells were imaged and calculated based on randomly selected
230 bright fields areas containing at least 200 cells per field as revelated by subsequent DAPI
231 staining.
232
233 **Cell Migration Assays**
234 AVICs were seeded in a 12-well plate at a concentration of $1x10^5$ cells per well and were left
235 until they reached 90% of confluence. The well surface was scratched with a 200 µl sterile
236 pipette tip and washed with PBS to remove detached cells. Horizontal lines were drawn on the
237 bottom outside of the well and used as a reference for alignment to obtain the same field for
238 each image acquisition run. VICs media was added, and images were collected at different time
239 points with a phase-contrast microscope using the horizontal lines as reference marks. Scratch

240 area and scratch width were determined with the Wound Healing Size Macro Tool using
241 ImageJ.[7] Linear regression and two-way ANOVA to compare the changes in the area and the
242 average length of the scratch.
243
244 **Chromatin Immunoprecipitation**
245 Chromatin Immunoprecipitation (ChIP) was performed on cultured cells as previously
246 described.[8] Briefly, AVICs were stimulated with osteogenic media for 14 days and then collected
247 in 20 mM Na-butyrate dissolved in PBS, and cross-linking of DNA and proteins was performed
248 with formaldehyde (1% vol/vol final concentration) at room temperature. Cross-linking was
249 stopped with 125 mM glycine for 10 min. Cross-linked chromatin was sonicated to obtain
250 fragments between 250 and 750 base pairs in a Bioruptor Pico sonication device (Diagenode).
251 The sheared chromatin was immunoprecipitated with 1 ug of antibody raised against TERT
252 (Rockland, 600-401-252S) and 0.3 ug STAT5 (Cell Signaling, 94205S). Normal rabbit polyclonal
253 IgG (Cell Signaling, 2729S) was used as a negative control. Negative control was incubated
254 with rabbit IgG and input DNA primary antibody. Chromatin complexes were recovered with
255 ChIP-grade Protein G magnetic beads (9006S, Cell Signaling). DNA was recovered with
256 standard phenol-chloroform extraction. Immunoprecipitated DNA was amplified by quantitative
257 RT-PCR using SYBR green. ChIP primers are listed in Supplementary Table 1.
258
259 **Proximity Ligation Assays (PLA)**
260 PLA was performed directly after cell fixation and according to manufacturer instructions. Briefly,
261 cells were blocked with Duolink blocking solution for 60 minutes at 37°C. Samples were then
262 incubated with rabbit TERT (Rockland) and mouse STAT5 (Santa Cruz) antibodies diluted in
263 Duolink Blocking Solution and incubated overnight at 4°C. Samples were then incubated with
264 secondary antibodies conjugated with PLA probes (DUO92002, DUO92004, Sigma) for 2 h at

265 37°C in a humidity chamber followed by probe ligation for 30 minutes at 37°C as recommended
266 by the manufacturer. Amplification was performed with Duolink detection kit Red 595 nm for 100
267 minutes at 37°C (DUO92101, Sigma). Samples were mounted in DAPI-containing mounting
268 media and prepared for image acquisition.
269
270 **Murine cell isolation**
271 *Tert* knockout mice (Jackson Labs, 005423) were bred with wild-type mice (Jackson Labs,
272 000664) to produce *Tert* heterozygous mice, which were then bred to each other to yield *Tert*
273 knockout mice and wild-type littermate controls. Het-het breeding ensures telomeres are intact.
274 Mouse BMMSCs were isolated from femurs and tibias were dissected from three-month-old
275 knockout or wild-type mice. The marrow was rinsed out of the bones with MSC media, and cells
276 were plated and expanded as described previously.[9] Mouse AVICs were isolated from hearts of
277 three-month-old *Tert* knockout or wild-type mice were removed, dissected, and valve leaflet
278 removed. Cells were isolated and expanded as described previously.[10] Mice were given
279 veterinary care by the University of Pittsburgh Division of Laboratory Animal Resources, which
280 adheres to the NIH policy on the Animal Welfare Act and all other applicable laws. Facilities are
281 under the full-time supervision of veterinarians and are AAALAC-accredited. Our protocols
282 follow the AVMA Guidelines on Euthanasia. All animal breeding and isolations were approved
283 by the Institutional Animal Care and Use Committee at the University of Pittsburgh. We made
284 attempts to minimize the number of mice required to complete experiments.
285
286 **Promoter Analysis**
287 The upstream region of the *RUNX2* (NM_001015051.3) promoter was scanned with LASAGNA[11]
288 and TRANSFAC/MATCH[12] suites. Searches were carried out with data version 2021.3, high

289 quality matrices and cut off to minimize false positives hits. STAT5 logo analysis was performed
290 with WebLogo (weblogo.berkeley.edu).
291
292 **Statistics**
293 Statistical analyses were performed with GraphPad Prism 9.2 (GraphPad Software, San Diego,
294 CA) software. All experiments used at least n = 3 biological replicates and were run in technical
295 duplicates. Statistical comparisons between the two groups were performed by a nonparametric
296 Mann-Whitney *U* test. Statistical comparisons among more than two groups were performed by
297 nonparametric Kruskal-Wallis *H* tests with post hoc Dunn's multiple pairwise comparisons
298 between groups or by Two-way ANOVA. Shapiro-Wilk normality test was used. to test data
299 distribution. Data are presented as mean ± standard deviation (SD).
300
301 **REFERENCES**

302 1. Cuevas RA, Chu CC, Moorhead Iii WJ, Wong R, Sultan I, St. Hilaire C. Isolation of
303 Human Primary Valve Cells for In vitro Disease Modeling. *JoVE*. 2021:e62439. doi:
304 doi:10.3791/62439
305 2. Cuevas RA, Chu CC, Moorhead WJ, 3rd, Wong R, Sultan I, St Hilaire C. Isolation of
306 Human Primary Valve Cells for In vitro Disease Modeling. *J Vis Exp*. 2021:e62439. doi:
307 10.3791/62439
308 3. Gupta GK, Dhar K, Del Core MG, Hunter WJ, 3rd, Hatzoudis GI, Agrawal DK.
309 Suppressor of cytokine signaling-3 and intimal hyperplasia in porcine coronary arteries
310 following coronary intervention. *Exp Mol Pathol*. 2011;91:346-352. doi:
311 10.1016/j.yexmp.2011.04.004
312 4. Hoemann CD, El-Gabalawy H, McKee MD. In vitro osteogenesis assays: influence of the
313 primary cell source on alkaline phosphatase activity and mineralization. *Pathol Biol*
314 *(Paris)*. 2009;57:318-323. doi: 10.1016/j.patbio.2008.06.004
315 5. Pascolo E, Wenz C, Lingner J, Hauel N, Priepke H, Kauffmann I, Garin-Chesa P, Rettig
316 WJ, Damm K, Schnapp A. Mechanism of human telomerase inhibition by BIBR1532, a

317 synthetic, non-nucleosidic drug candidate. *J Biol Chem*. 2002;277:15566-15572. doi:
318 10.1074/jbc.M201266200
319 6. Cawthon RM. Telomere measurement by quantitative PCR. *Nucleic Acids Res*.
320 2002;30:e47. doi: 10.1093/nar/30.10.e47
321 7. Suarez-Arnedo A, Torres Figueroa F, Clavijo C, Arbelaez P, Cruz JC, Munoz-Camargo
322 C. An image J plugin for the high throughput image analysis of in vitro scratch wound
323 healing assays. *PLoS One*. 2020;15:e0232565. doi: 10.1371/journal.pone.0232565
324 8. Dahl JA, Collas P. A rapid micro chromatin immunoprecipitation assay (microChIP). *Nat*
325 *Protoc*. 2008;3:1032-1045. doi: 10.1038/nprot.2008.68
326 9. Huang S, Xu L, Sun Y, Wu T, Wang K, Li G. An improved protocol for isolation and
327 culture of mesenchymal stem cells from mouse bone marrow. *J Orthop Translat*.
328 2015;3:26-33. doi: 10.1016/j.jot.2014.07.005
329 10. Bouchareb R, Lebeche D. Isolation of Mouse Interstitial Valve Cells to Study the
330 Calcification of the Aortic Valve In Vitro. *J Vis Exp*. 2021. doi: 10.3791/62419
331 11. Lee C, Huang CH. LASAGNA: a novel algorithm for transcription factor binding site
332 alignment. *BMC Bioinformatics*. 2013;14:108. doi: 10.1186/1471-2105-14-108
333 12. Wingender E, Dietze P, Karas H, Knuppel R. TRANSFAC: a database on transcription
334 factors and their DNA binding sites. *Nucleic Acids Res*. 1996;24:238-241. doi:
335 10.1093/nar/24.1.238
336

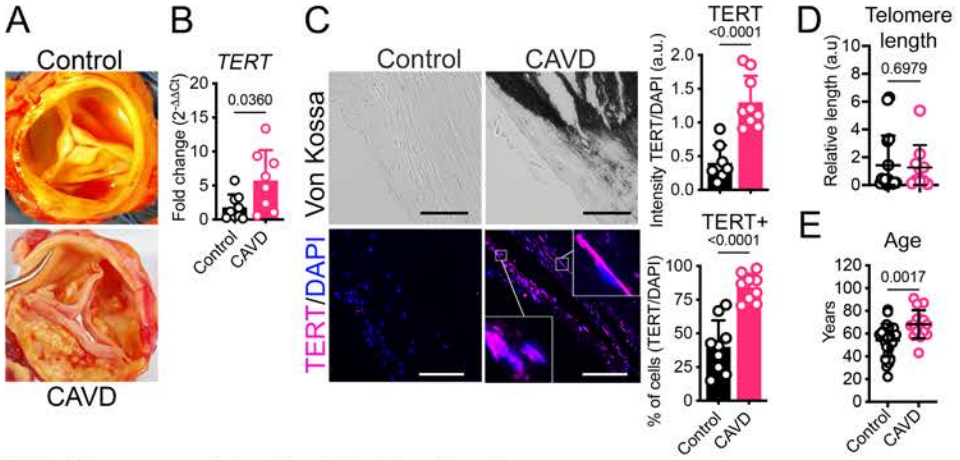

Figure 1. TERT is upregulated in CAVD valve tissue.
A, Surgically removed specimen of control (top) and CAVD (bottom) human valves. B, TERT mRNA transcript quantification in control and CAVD valve tissues. n = 8 control, n= 9 CAVD. C, Representative serial sections of Von Kossa (dark precipitation, top panels) and TERT immunofluorescent staining (bottom panels) in control and CAVD valve tissues. Scalebar 100 µm. Quantification of TERT intensity and the number of TERT-positive cells on the leaflet is shown on the right graphs. n = 9 control, n = 9 CAVD. D, Telomere length measurements in valve tissues. n = 16 control, n = 10 CAVD. E. Age of the patients utilized in this study. n = 25 control, n = 16 CAVD. Data are shown as means ± SD. *P* values were calculated by the Mann-Whitney *U* test and shown on each graph.

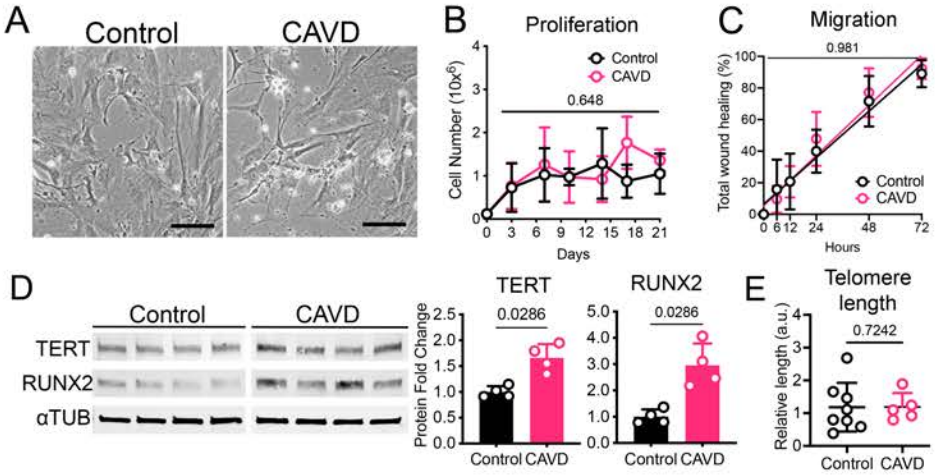

Figure 2. Valve interstitial cells isolated from CAVD patients show elevated TERT expression at baseline.

A, Representative images showing cell morphology of control (left) and CAVD (right) VICs. Scalebar 50 μm. B, Proliferation of control and CAVD VICs at baseline. n = 3 control, n = 3 CAVD. Data represents means ± SD. C, Relative migration distances of control and CAVD VICs. n = 10 control, n = 10 CAVD. Representative western blot staining of control and CAVD VICs at baseline. Quantification of protein levels is shown on the right panels. n = 4 control, n = 4 CAVD/. E, Telomere length measurements in VICs. n = 8, control, n = 5 CAVD; means ± SD. Data are shown as means ± SD. *P* values were calculated by the Mann-Whitney *U* test and shown on each graph.

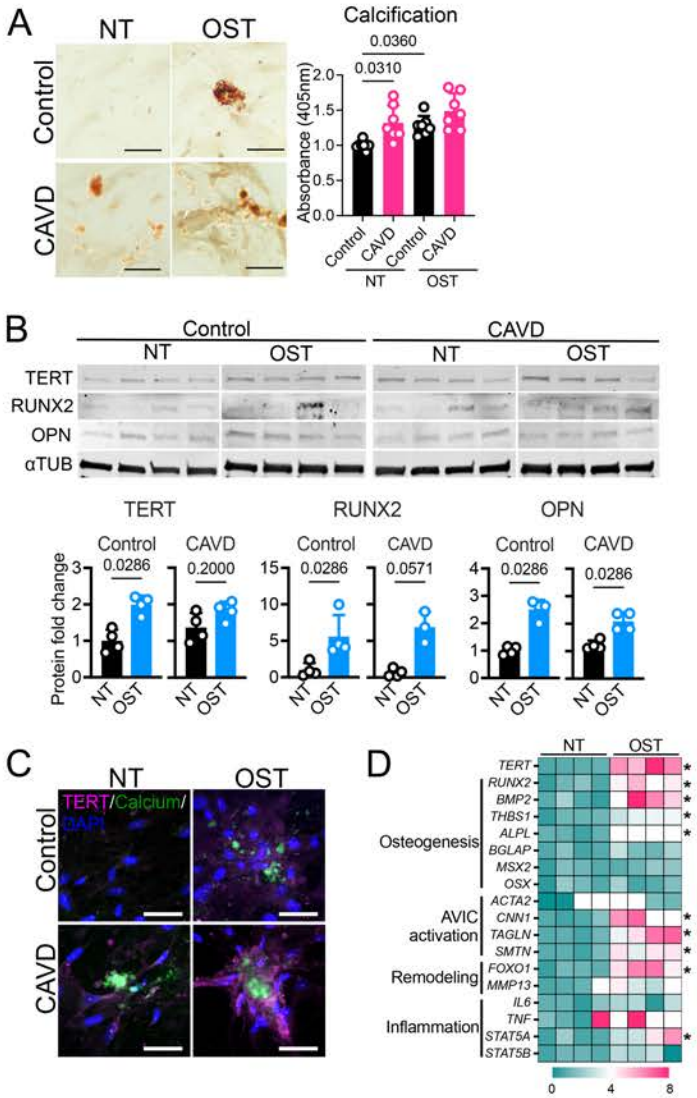

Figure 3. TERT is upregulated during osteogenic differentiation of VICs.
A, Representative images of VICs growing in normal conditions (no treatment, NT, left panel) or stimulated with osteogenic media (OST) for 14 days. Calcium deposition was visualized by Alizarin Red staining. Scalebar 50 µm. Quantification of calcification is shown as average absorbance ± SD on the right graphs. n = 7 control, n = 7 CAVD. B, Representative western blot staining of samples from control and CAVD VICs after 14 days of NT or OST. Quantification of protein levels is shown on the right graphs. n = 4 control, n = 4 CAVD. C, Representative immunofluorescent staining images of TERT in control and CAVD VICs after 14 days of NT or OST. Calcium deposition was visualized by OsteoImage staining. Scalebar 100 µm. D. Expression profile control VICs after 14 days of NT and OST treatment. n = 4 NT, n = 4 OST. Data are shown as means ± SD. *P* values were calculated by the Mann-Whitney *U* test with * *P* = 0.0286 in Figure D.

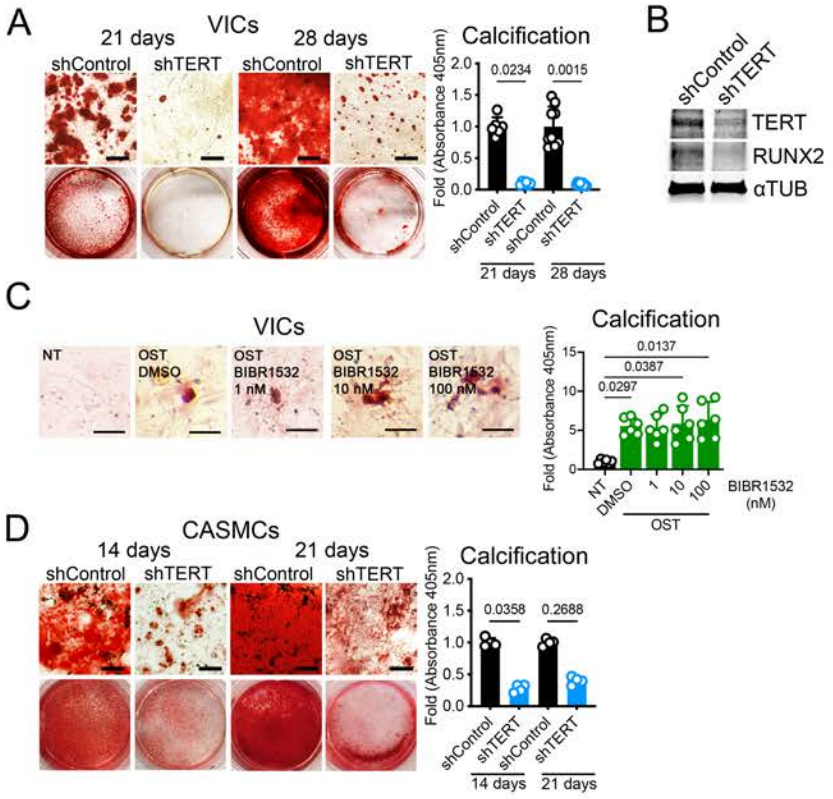

Figure 4. TERT is required for osteogenic transition and calcification of human cells.
A, VICs transduced with lentivirus containing either short hairpin scramble (shControl-GFP) or short hairpin TERT (shTERT-GFP) and followed by OST stimulated for up to 28 days. Calcium deposition was visualized by Alizarin Red staining. Quantification of calcification is presented as average absorbance on the right graph. n = 6 shControl, n = 6 shTERT at 21 days and n = 9 shControl, n = 9 shTERT at day 28. Scalebar 400 µm. Data are shown as means ± SD.
B, Representative western blot staining of VICs transduced with lentivirus containing either shControl-GFP or shTERT-GFP followed by 7 days of osteogenic stimulation. C. VICs treated with BIBR1532 and stimulated with osteogenic media for 28 days. Scalebar 50 µm. Quantification of calcification is shown on the right graph. n = 6. Data are shown as means ± SD. D, CASMCs transduced with lentivirus containing either shControl-GFP or shTERT-GFP and stimulated with osteogenic media for up to 21 days. n = 4 shControl, n = 4 shTERT for both time points. Scalebar 400 µm. Quantification of calcification is shown on right graph. *P* values were calculated with the Kruskal-Wallis *H* test with Dunn post hoc test and shown on top of each graph.

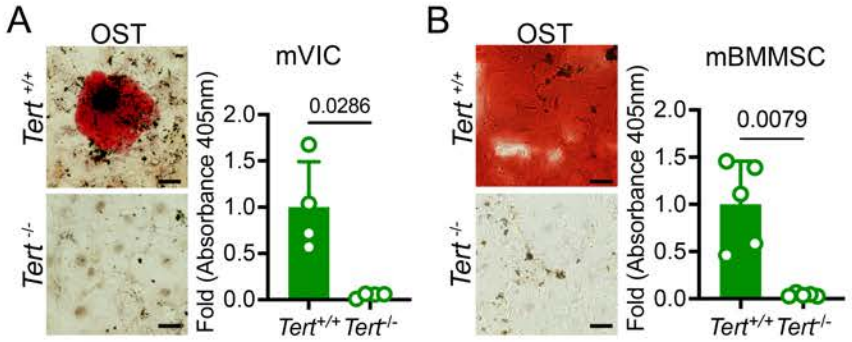

Figure 5. TERT is required for the osteogenic transition of murine cells.
A, Representative images of mVICs isolated from wild-type (*Tert* $^{+/+}$) or F1 *Tert* knockout (*Tert* $^{-/-}$) mice and stimulated with osteogenic media for 21 days. Scalebar 100 µm. Quantification of calcification is shown on the right graph. B, Representative images of mBMMSCs isolated from *Tert* $^{+/+}$ or *Tert* $^{-/-}$ mice and stimulated with osteogenic media for 21 days. Scalebar 100 µm. Quantification of calcification is presented as average absorbance on the right graphs. All graphs are n = 4 *Tert* $^{+/+}$, n = 4 *Tert* $^{-/-}$. Data are shown as means ± SD. *P* values were calculated by the Mann-Whitney *U* test and indicated on each graph.

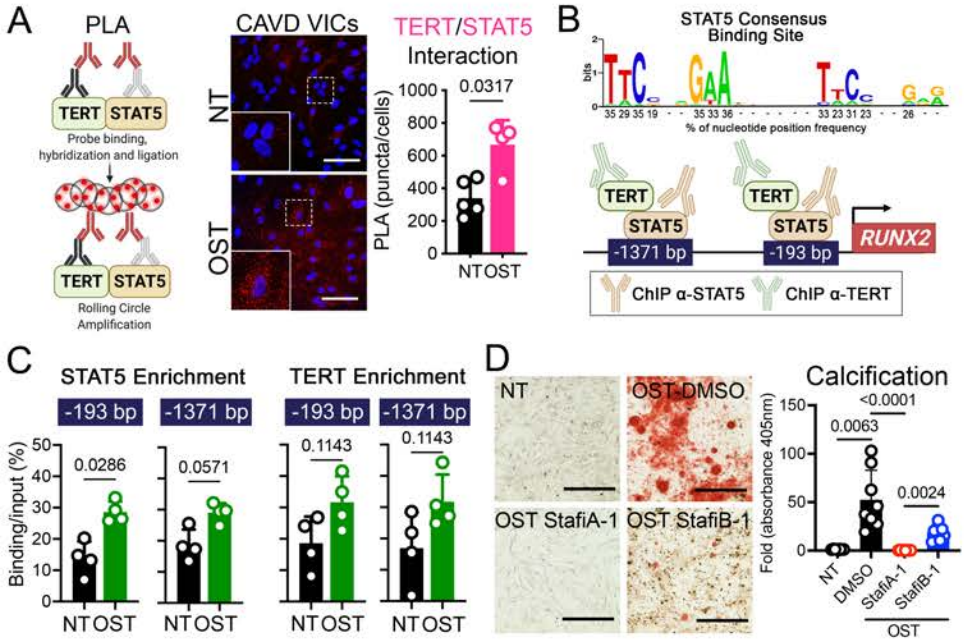

Figure 6. TERT and STAT5 interact to upregulate RUNX2 expression in human VICs. A, Diagram of proximity ligation assay (PLA, left panel). Representative images of TERT/STAT5 complex (red foci) in CAVD VICs cultured for 21 days in osteogenic medium and detected by PLA. Scalebar 100 μm (middle panel). Quantification of PLA signal is shown in the right graph. n = 4. B, Logo analysis depicting the consensus binding site for tetrameric STAT5 (top panel). Diagram depicting STAT5 and TERT binding RUNX2 promoter and the positions of the predicted STAT5 binding sites (bottom panel). C, STAT5 (left graphs) and TERT (right graphs) enrichment on the RUNX2 promoter of control VICs after 14 days of osteogenic stimulation and quantified by ChIP-qPCR. n = 4. D, Representative images of control and CAVD VICs treated with 10 μM of the STAT5 inhibitors StafiA-1or StafiB-1 during 28 days of osteogenic stimulation. Scalebar 400 μm. n = 8, means ± SD. Quantification of calcification is shown on the right graph. Data are shown as means ± SD. P values were calculated by the Mann-Whitney U test (Figure A and C) and Kruskal-Wallis H test (Figure D) and indicated on each graph.

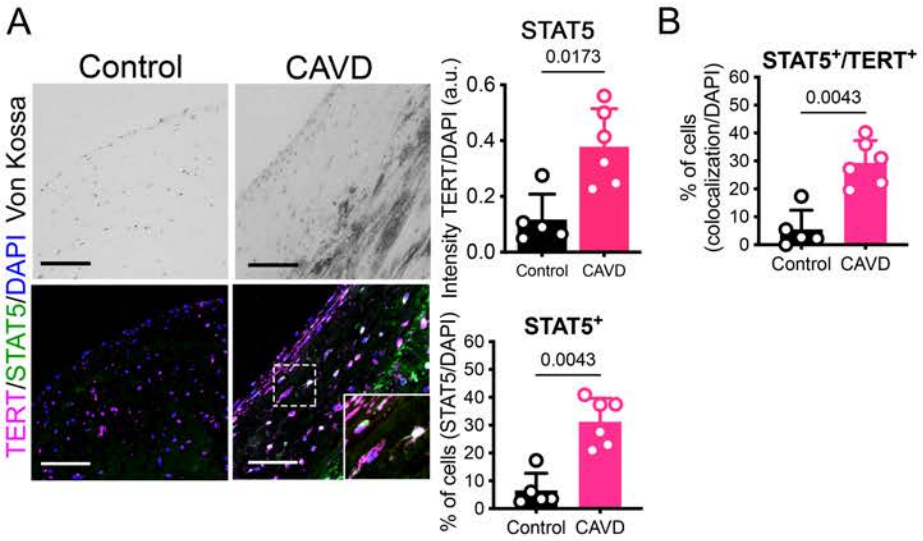

Figure 7. TERT and STAT5 are upregulated and colocalize in CAVD tissue.
A, Representative serial sections of Von Kossa (dark precipitation, top panels) and TERT and STAT5 immunofluorescent staining (bottom panels) in control and CAVD valve tissues. Scalebar 100 µm. Quantification of STAT5 intensity and STAT5-positive cells (STAT5+) are shown on the right panels. B, Quantification of STAT5-TERT-positive cells. Data are shown as means ± SD, n = 5 control, n = 6 CAVD. *P* values were calculated with the Mann-Whitney *U* test and indicated on each graph.

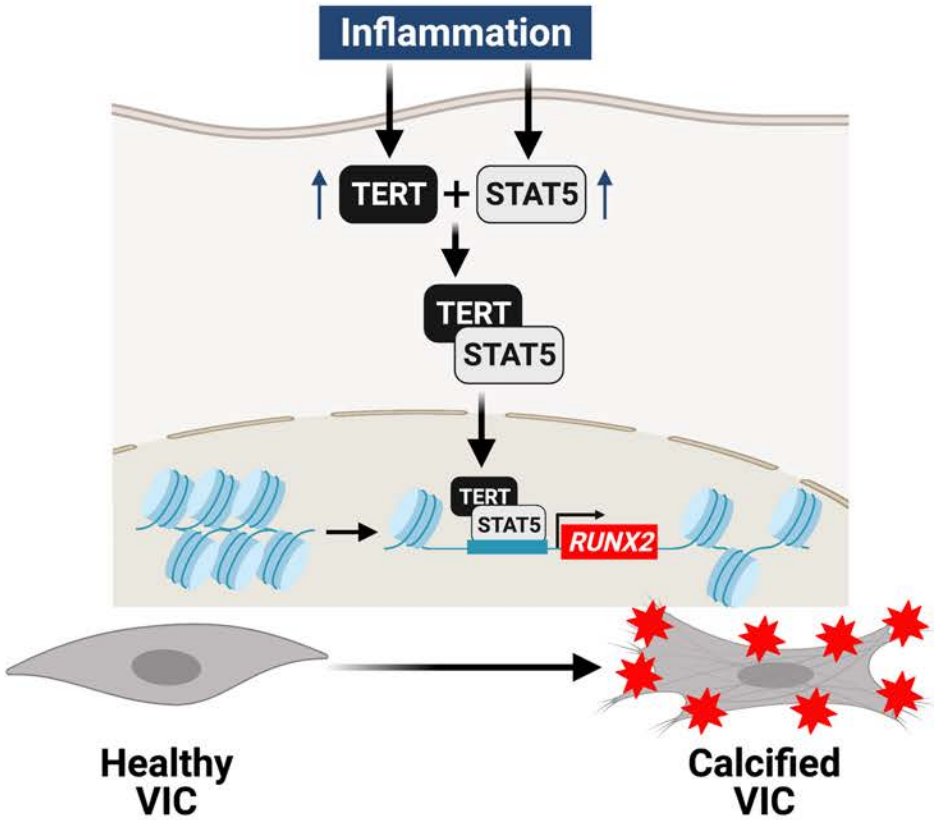

Figure 8. TERT/STAT5 promotes osteogenic reprogramming
Inflammation promotes the upregulation and interaction of TERT and STAT5. Then, the TERT/STAT5 complex translocates into the nucleus where TERT facilitates STAT5 binding to the promoter region of *RUNX2* gene, to engage the osteogenic reprogramming of VICs during the early stages of CAVD pathogenesis.

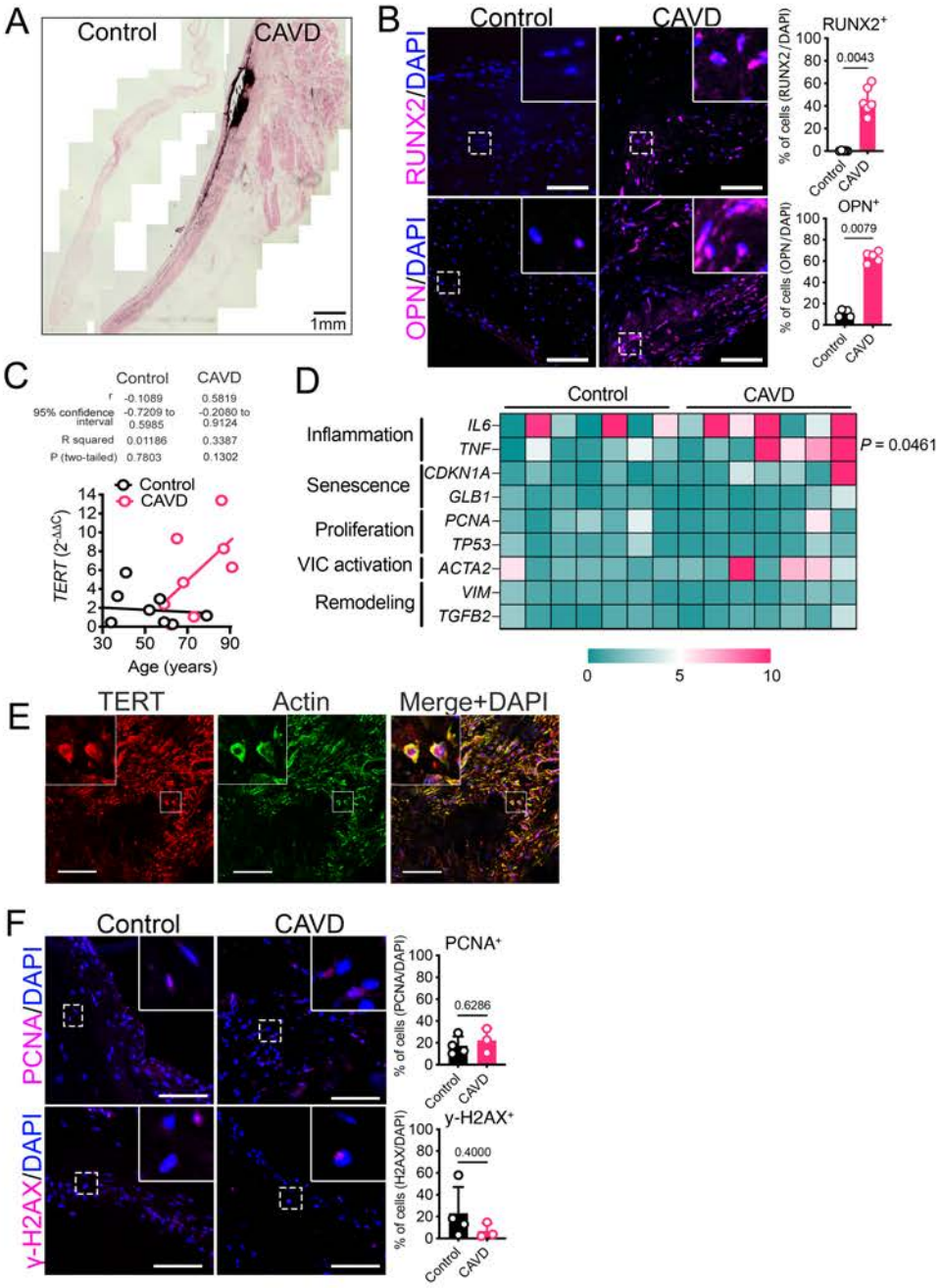

Supplemental Figure 1. Characterization of human CAVD valves and correlation of TERT expression with age.

A, Representative section of Von Kossa staining in control and valve CAVD leaflets tissue. Scalebar 1 mm. B, Representative serial sections of RUNX2 immunofluorescent staining (top panels) and OPN (bottom panels) in control and CAVD valve tissues. Scalebar 100 μm. Quantification of RUNX2-positive cells and OPN-positive cells on the leaflet specimen is shown on the right graphs. n = 5 control, n = 6 CAVD. C, Correlation between age of the donor and *TERT* expression. n = 8 control, n = 9 CAVD, Pearson correlation test. D, Expression profile in the subject leaflets. n = 7 control, n = 7 CAVD. E, Confocal images of a CAVD leaflet. Scalebar 50 μm. F, Representative images of immunofluorescent staining of PCNA (top panels) and γ-H2AX (bottom panels) in control and CAVD valve tissues. Scalebar 100 μm. Quantification of PCNA-positive cells and γ-H2AX-positive cells are shown on the right graphs. n = 4 control, n = 3 CAVD. Data are showns as means ± SD. *P* values were calculated with the Mann-Whitney *U* test (Figures B, G, and F) and two-way ANOVA with Sidak post hoc test (heatmap on D).

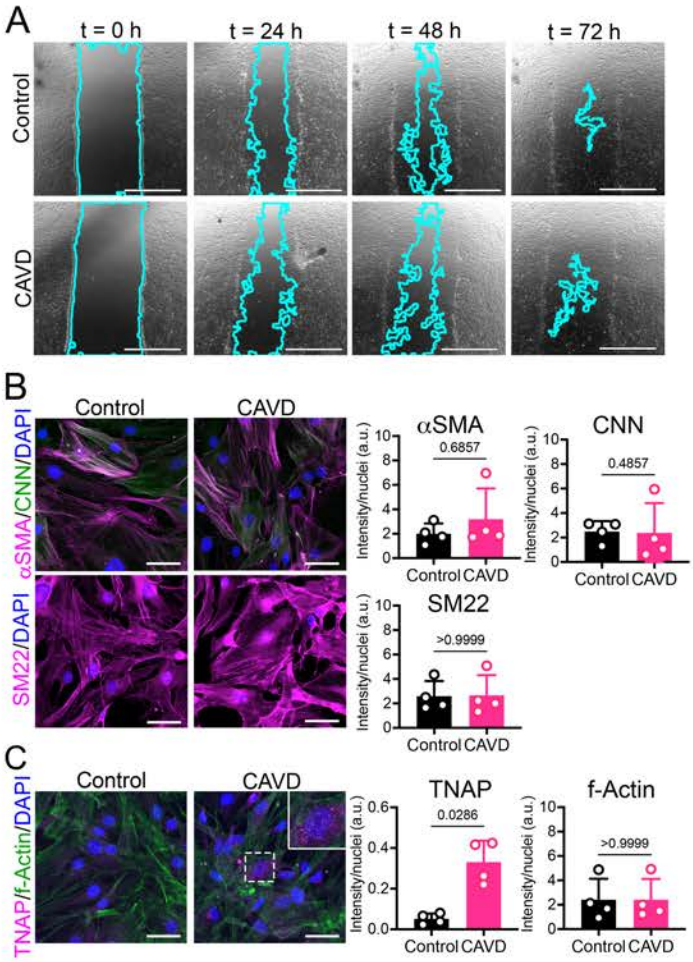

Supplemental Figure 2. VIC migration, activation, and osteogenic markers at baseline. A, Representative images of a scratch assay in control (top panels) and CAVD (bottom panels) VICs. Time points are indicated on top of each panel. Blue lines denote the cell migration front. Scalebar 1 mm. n = 10 control, n = 10 CAVD. B, Representative images of αSMA and CNN (top panels) and SM22 (bottom panels) in control and CAVD VICs. Scalebar 50 μm. Signal quantification of αSMA, CNN, and SM22 are shown on the right panels. n = 4 control, n = 4 CAVD. C, Representative images of TNAP and f-Actin signal in control and CAVD VICs. Scalebar 50 μm. Signal quantification of TNAP and f-Actin is shown on the right panels. n = 4 control, n = 4 CAVD. Data are shown as means ± SD. *P* values were calculated with the Mann-Whitney *U* test and shown on top of each graph.

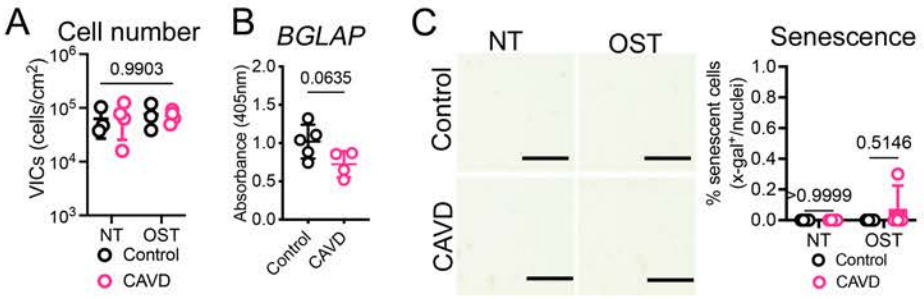

Supplemental Figure 3. Senescence is not operative during the osteogenic differentiation of VICs.

A, Cell counting of control and CAVD VICs after 14 days of NT or OST stimulation. n = 4 control, n = 4 CAVD. B, β-galactosidase (*BGLAP*) mRNA transcript quantification in control and CAVD VICs at baseline. n = 5 control, n= 4 CAVD. C, Representative images of senescence-associated β-galactosidase activity staining of VICs after 28 days of NT or OST stimulation. Blue cells were considered positive for senescence. Quantification of senescence is shown on the right graph. n = 4 control; n = 4 CAVD. Data are shown as means ± SD. *P* values were calculated with the Mann-Whitney U test (figure A and B) and the Kruskal-Wallis *H* test with Dunn post hoc test and shown on top of each graph.

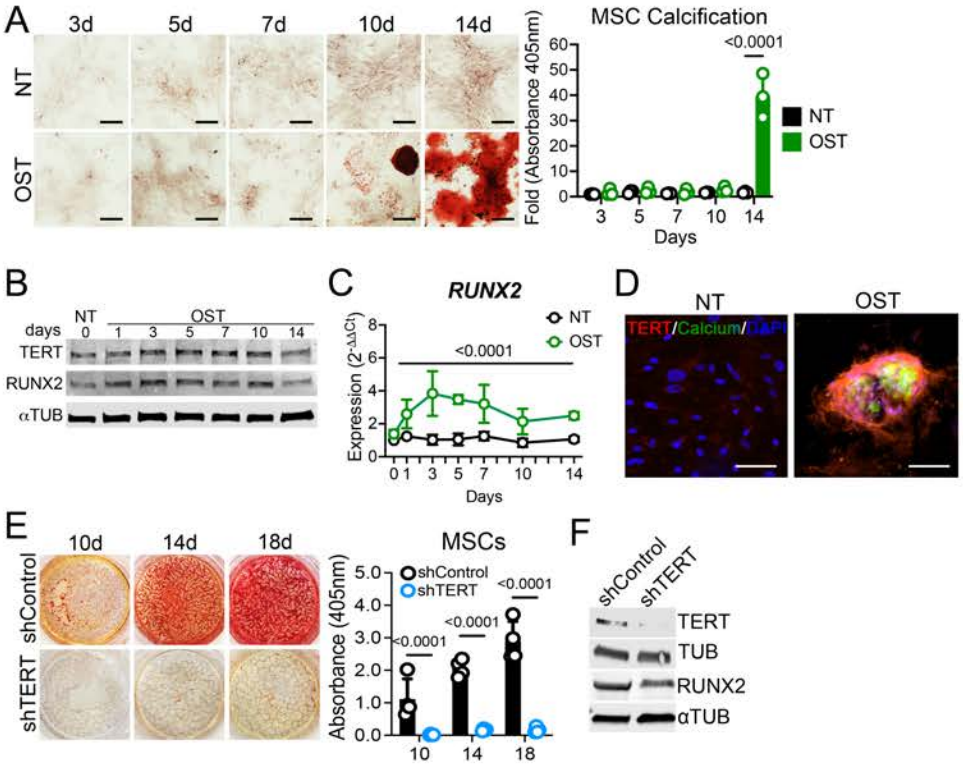

Supplemental Figure 4. TERT is upregulated and required for the osteogenic differentiation of human mesenchymal stem cells.

A, Representative images of human MSCs stimulated with OST for 14 days. Calcium deposition was visualized by Alizarin Red staining. Quantification of calcification is shown on the right graph. n = 3. Scalebar 50 μm. B, Western blot staining of samples from MSCs collected during the 14 days of OST treatment. C, TERT and RUNX2 expression profile of differentiating MSCs stimulated for 14 days with OST media. n = 3. D, Representative TERT immunofluorescent staining images of MSCs stimulated with osteogenic media for 14 days. Scalebar 100 μm. E, MSCs transduced with lentivirus containing either shControl-GFP or shTERT-GFP and stimulated with osteogenic media for up to 21 days. Quantification of calcification is shown on the right graph. n = 4; means ± SD. F, Representative western blot staining of MSCs transduced with lentivirus containing either shControl-GFP or shTERT-GFP followed by 7 days of osteogenic stimulation. Data are shown as means ± SD. *P* values were calculated by Kruskal-Wallis *H* test with Dunn pairwise comparison post hoc test (Figure C) and two-way ANOVA with Tukey post hoc test (Figures A and E).

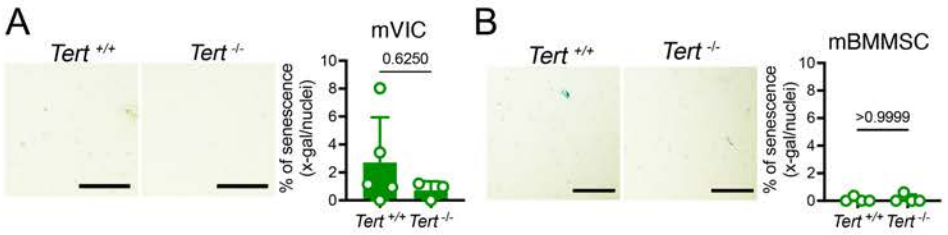

Supplemental Figure 5. Senescence is not operative in mice *Tert* $^{-/-}$ cells.
A, Representative images of a senescence-associated β-galactosidase (SA-β-gal) staining of mVICs isolated from wild-type (*Tert* $^{+/+}$) or F1 *Tert* knockout (*Tert* $^{-/-}$) mice after 21 days of OST stimulation. Blue cells were considered positive for senescence. Quantification of senescence cells is shown on the right graph. B, Representative images of SA-β-gal staining of mBMMSCs isolated from *Tert* $^{+/+}$ or *Tert* $^{-/-}$ mice after 21 days of osteogenic stimulation. Blue cells were considered to be positive for senescence. Quantification of senescence is shown on the right graph. Both figures, n = 5 *Tert* $^{+/+}$, n = 3 *Tert* $^{-/-}$. Scalebar 400 μm. Data are shown as means ± SD and *P* were calculated with the Mann-Whitney *U* test and shown on each graph.

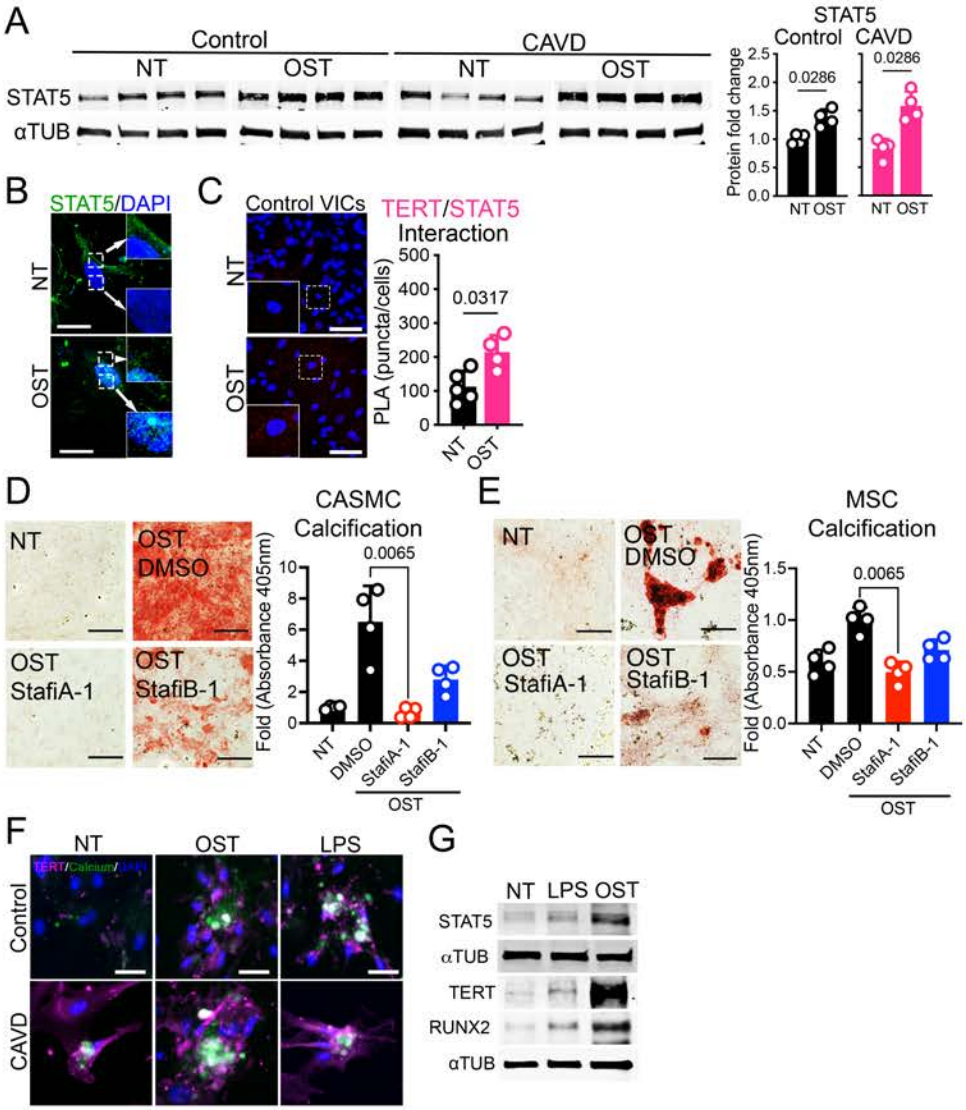

Supplemental Data Fig 6. STAT5 is upregulated and required during osteogenic differentiation of VICs.

A, Representative western blot staining of samples from CAVD and control VICs after 14 days of OST stimulation. Quantification of protein levels is shown on the right graphs. n = 4, control n = 4 CAVD. B, Representative immunofluorescence image of STAT5 shows subcellular distribution after 14 days of NT and OST stimulation. Scalebar 40 µm. C, Representative images of TERT/STAT5 complex (red foci) in control VICs and detected by proximity ligation assay (PLA). Scalebar 100 µm. Quantification of PLA is shown on the right graph. n = 4. D, Representative images of CASMCs (left panels) treated with 10 µM of the STAT5 inhibitors StafiA-1 or StafiB-1 during the 14 days of OST stimulation. Scalebar 400 µm. Quantification of calcification is shown on the right graph. n = 4. E, Representative images of MSCs (left panels) treated with 10 µM of the STAT5 inhibitors StafiA-1 or StafiB-1 during the 21 days of OST stimulation. Scalebar 400 µm. Quantification of calcification is shown on the right graph. n = 4. F, Representative immunofluorescence images of VICs after 14 days of LPS treatment or OST stimulation. Scalebar 50 µm. G, Representative western blot staining of CAVD VICs after 14 days of OST stimulation. Data are shown as means ± SD. *P* values were calculated with the Mann-Whitney *U* test (Figures A and B) and the Kruskal-Wallis *H* test with Dunn pairwise comparison post-test (Figured D and E) and indicated in each graph.

Table 1: Patient information

Patient ID	Age	Sex	Cause of Death	Calcification (Von Kossa Staining)	Hypertension	Diabetes	Smoking	Alcohol
2016-037	31	Male	Brain anoxia due to cardiovascular complications	No	No	No	Unknown	Yes
2016-038	81	Male	Myocardial Infarction	No	No	No	Unknown	Unknown
2016-042	22	Female	Brain anoxia due to head trauma	No	No	No	No	Unknown
2016-045	59	Female	Stroke	No	PH	Yes	Yes	Unknown
2016-046	65	Male	Head trauma from accident	No	No	No	Unknown	Unknown
2016-048	56	Female	Stroke	No	HTN	No	Unknown	Unknown
2016-050	65	Male	Stroke	No	HTN	No	Unknown	Yes
2016-054	63	Female	Hemorriage and Ruptire AAA	No	No	Yes	No	Unknown
2016-065	58	Male	Stroke	No	HTN	Yes	Yes	Unknown
2016-073	41	Female	Traumatic arrest and motor vehicle accident	No	HTN	No	Yes	Unknown
2016-078	34	Female	Heart Failure	No	No	No	Unknown	Unknown
2016-079	59	Male	Respiratory failure	No	HTN	No	No	Unknown
2016-083	52	Male	Stroke	No	PAH	No	Yes	Unknown
2016-085	52	Male	Myocardial Infarction	No	PH	No	Unknown	Unknown
2016-091	59	Female	Stroke	No	HTN	No	Unknown	Unknown
2016-092	47	Female	Stroke	No	No	No	No	Unknown
2016-098	57	Male	Cardiac arrest	No	HTN	No	Yes	Unknown
2016-101	37	Female	Cardiac Death	No	No	No	Unknown	Unknown
2016-146	79	Male	Cardiac arrest	No	No	No	Yes	Unknown
2017-005	66	Female	Stroke	No	No	No	Unknown	Unknown
2017-035	48	Female	Brain anoxia due to CO poisoning	No	No	No	Unknown	Unknown
2017-051	56	Male	Brain anoxia due to cardiac arrest	No	No	No	Unknown	Unknown
2017-069	37	Male	Motor vehicle accident	No	No	No	Unknown	Unknown
03-0127	61	Male	Surgical replacement due to aortic reconstruction for aneurysm	No	HTN	No	Unknown	Unknown
03-0129	68	Male	Surgical replacement due to aortic reconstruction for aneurysm	No	HTN	Yes Type II	Unknown	Unknown
2016-034	91	Male	Natural causes	Yes	No	No	No	Unknown
2016-051	65	Male	Natural causes	Yes	HTN	No	Yes	Yes
2016-053	73	Male	Congestive heart failure	Yes	No	No	No	Unknown

2016-060	73	Male	Cardiac arrest	Yes	No	No	Unknown	Unknown
2016-061	67	Male	Natural causes	Yes	No	Yes	Unknown	Unknown
2016-062	59	Male	Cardiac arrest	Yes	No	No	Yes	Unknown
2016-068	68	Female	Intracranial hemorrhage	Yes	No	No	Yes	Unknown
2016-072	62	Female	Cardiac arrest	Yes	No	No	No	Unknown
2016-093	43	Male	Cardiac arrest	Yes	HTN	Yes	No	Unknown
2016-095	87	Male	Myocardial Infarction	Yes	HTN	No	Yes	Unknown
2016-102	58	Female	Cardiac arrest and asystole	Yes	No	No	Yes	Unknown
2016-103	72	Male	Cardiac arrest	Yes	HTN	No	Unknown	Unknown
2016-105	86	Male	Cardiac arrest	Yes	No	No	No	Unknown
2016-118	62	Male	Cardiac arrest	Yes	No	No	No	Unknown
2017-025	57	Female	Brain anoxia due to choking	Yes	No	Yes Type II	Unknown	Unknown
2017-076	68	Female	Myocardial Infarction	Yes	No	No	No	Unknown

HTN = Hypertension PH = Pulmonary Hypertension PAH = Pulmonary Arterial Hypertension

Table 2: Patient Summary

Summary	total	age	% male	% hypertension	% CVD death	% deceased
control	25	54	52%	48%	68%	100%%
calcified	16	68	81%	25%	81%	100%

Supplemental Table 1: TRANSFAC STAT5 Binding Sites on RUNX2 promoter

Transcription Factor	Position	Core score	Matrix score	Sequence
STAT5A (homodimer)	-4571	1	0.948	ctTTTCCaagaaagc
STAT5B (homodimer)	-4571	0.968	0.954	cttttccaAGAAAgc
STAT5B:STAT5A	-4570	1	0.999	ttTTCCAagaa
STAT5A	-4570	1	0.994	ttttccAAGAAag
STAT5A	-4568	1	1	TTCCAagaaa
STAT5A (homotetramer)	-4568	0.996	0.846	ttccaAGAAAgctaatatacaaaa
STAT5A	-3801	1	1	tAGAAAtg
STAT5A	-3035	1	1	tAGAAAtg
STAT5A (homotetramer)	-2843	0.996	0.866	taccaacaacttttTTTCTttgaa
STAT5A (homotetramer)	-2828	0.977	0.899	ttcttTGAAAttgatttcaagatc
STAT5A (homotetramer)	-2875	0.977	0.873	gggtttgtaagatgTTTCAgtgaa
STAT5A (homotetramer)	-1371	0.788	0.834	taaatggcaaaaaaATGCCtagaa
STAT5A (homotetramer)	-193	0.995	0.882	tgccaGGAAAggccttaccacaag

Supplementary Table 2: Primers

Species	Gene	Forward Primer Sequence 5' -> 3'	Reverse Primer Sequence 5' -> 3'	Techniq	Source
Human	TERT	GCATTGGAATCAGACAGCAC	CCACGACGTAGTCCATGTTC	qPCR	Sigma-Aldrich
Human	RUNX2	ATTCCTGTAGATCCGAGCACC	GCTCACGTCGCTCATTTTGC	qPCR	IDT
Human	MSX2	GAGCTGGGATGTGGTAAAGG	AAATTCAGAAGATGGAGCGG	qPCR	IDT
Human	CDKN1A	TGTCCGTCAGAACCCATG	AAAGTCGAAGTTCCATCGCTC	qPCR	IDT
Human	PCNA	ACACTAAGGGCCGAAGATAAC	ACAGCATCTCCAATATGGCTGA	qPCR	IDT
Human	TP53	GAGGTTGGCTCTGACTGTACC	TCCGTCCCAGTAGATTACCAC	qPCR	IDT
Human	ALPL	ATGGGATGGGTGTCTCCACA	CCACGAAGGGGAACTTGTC	qPCR	IDT
Human	GLB1	TATACTGGCTGGCTAGATCACTG	GGCAAAATTGGTCCCACCTATAA	qPCR	IDT
Human	STAT3	CAGCAGCTTGACACACGGTA	GCCCAATCTTGACTCTCAATCC	qPCR	IDT
Human	STAT5A	ATGTGAAACCACAGATCAAG	TCTGTGGGTACATGTTATAGG	qPCR	Sigma-Aldrich
Human	STAT5B	ATGGGACTCAGTAGATCTTG	CTTCAGTAAAAACCCATCTTCC	qPCR	Sigma-Aldrich
Human	TGFb2	CTGCATCTGGTCACGGTCG	CCTCGGGCTCAGGATAGTCT	qPCR	IDT
Human	OSX	CCCCCTTTACAAGCACTAATGG	GGCAGACAGTCAGAAGAGCTG	qPCR	IDT
Human	ACTA2	AAAAGACAGCTACGTGGGTGA	GCCATGTTCTATCGGGTACTTC	qPCR	IDT
Human	FOXO1	TCGTCATAATCTGTCCCTACACA	CGGCTTCGGCTCTTAGCAAA	qPCR	Sigma-Aldrich
Human	18s	GTAACCCGTTGAACCCCATT	CCATCCAATCGGTAGTAGCG	qPCR	IDT
Human	MYH11	CGCCAAGAGACTCGTCTGG	TCTTTCCCAACCGTGACCTTC	qPCR	IDT
Human	IL6	AAATTCGGTACATCCTCGACGG	GGAAGGTTCAGGTTGTTTTCTGC	qPCR	IDT
Human	VIM	GGAAACTAATCTGGATTCACTC	CATCTCTAGTTTCAACCGTC	qPCR	Sigma-Aldrich
Human	SOX9	GCCAGGTGCTCAAAGGCTA	TCTCGTTCAGAAGTCTCCAGAG	qPCR	IDT
Human	KLF4	CCCACATGAAGCGACTTCCC	CAGGTCCAGGAGATCGTTGAA	qPCR	IDT
Human	SM22	AGTGCAGTCCAAAATCGAGAAG	CTTGCTCAGAATCACGCCAT	qPCR	IDT
Human	TNF	CCTCTCTCTAATCAGCCCTCTG	GAGGACCTGGGAGTAGATGAG	qPCR	IDT
Human	BGLAP	GGACTGTGACGAGTTGGCTG	CCGTAGAAGCGCCGATAGG	qPCR	IDT
Human	SMTN	CAAAAAGTCCTAACCCCTGCT	TCATGTCGTCCACCTCCAC	qPCR	IDT
Human	BMP2	ACCCGCTGTCTTCTAGCGT	TAAATTGAAGAAGAAGCGCC	qPCR	Sigma-Aldrich
Human	THBS1	TGCTCCAATGCCACAGTTCC	CTGCTGAATTCCATTGCCACA	qPCR	IDT
Human	CNN1	GTCAACCCAAAATTGGCACCA	ACCTTGTTTCCTTTCGTCTTCG	qPCR	IDT
Human	MMP13	CACCAATTCCTGGGAAGTCT	GCAGCTGTTCACTTTGAGGA	qPCR	IDT
Human	GAPDH	CTGGGCTACACTGAGCACC	AAGTGGTCGTTGAGGGCAATG	qPCR	IDT
Human	pRUNX2-1	ACCTTACAGGAGTTTGGGCT	CTTTCCTGGCATCCAGAAGGATA	ChIP	IDT
Human	pRUNX2-2	CCGCCCACCCCATTTACTT	GGCGAACAGACCAATTTTCTAGG	ChIP	IDT
Human	hTelomere	GGTTTTTGAGGGTGAGGGTGAGGGT	TCCCGACTATCCCTATCCCTATCCCT	PCR	Sigma-Aldrich